Research Square

Preprints are preliminary reports that have not undergone peer review.
They should not be considered conclusive, used to inform clinical practice,
or referenced by the media as validated information.

A cortex-wide self-consistent manifold for a body–environment reference frame

Riichiro Hira

riichirohira@gmail.com

Institute of Science Tokyo https://orcid.org/0000-0002-8719-4498

Fumiya Imamura

Institute of Science Tokyo

Hiroto Imamura

Tokyo medical and dental university

Reiko Hira

Institute of Science Tokyo https://orcid.org/0009-0006-4729-4925

Yoshikazu Isomura

Department of Physiology and Cell Biology, Graduate School of Medical and Dental Sciences, Tokyo Medical and Dental University https://orcid.org/0000-0003-0393-3124

Article

Keywords:

Posted Date: June 3rd, 2026

DOI: https://doi.org/10.21203/rs.3.rs-9592609/v1

License: This work is licensed under a Creative Commons Attribution 4.0 International License.
Read Full License

Additional Declarations: There is **NO** Competing Interest.

A cortex-wide self-consistent manifold for a body–environment reference frame

Fumiya Imamura[1], Hiroto Imamura[1], Reiko Hira[1], Yoshikazu Isomura[1,†], Riichiro Hira[1,2,†]

Affiliations:

1. Department of Physiology and Cell Biology, Graduate School of Medical and Dental Sciences, Institute of Science Tokyo, Tokyo, Japan

2. High Performance Artificial Intelligence System Research Team, Center for Computational Science, RIKEN, Saitama 351-0198, Japan

[†] Corresponding authors.

Correspondence:

Riichiro Hira, M.D., Ph.D. rhira.phy2@tmd.ac.jp

Department of Physiology and Cell Biology, Graduate School of Medical and Dental Sciences, Institute of Science Tokyo, 1-5-45 Yushima, Bunkyo-ku, Tokyo, 113-8510, Japan.

Yoshikazu Isomura, Ph.D. isomura.phy2@tmd.ac.jp

Department of Physiology and Cell Biology, Graduate School of Medical and Dental Sciences, Institute of Science Tokyo, 1-5-45 Yushima, Bunkyo-ku, Tokyo, 113-8510, Japan.

Abstract

Ground-tilt provides a fundamental reference frame for stabilizing posture, interpreting sensory inputs and planning actions [1–5]. Although cortical contributions to posture and balance are well recognized [6–11], it remains unclear how ground-tilt itself is represented across the cortex, including frontal, parietal, primary sensory, and motor cortices. Here, we developed a system that delivers arbitrary patterns of ground motion to head-fixed mice while enabling simultaneous large-field-of-view two-photon calcium imaging across dorsal cortical areas. Although encoding-model-based analysis showed that tilt selectivity was concentrated in the posterior parietal cortex, tilt information could be decoded from all recorded cortical areas. Population analyses revealed that tilt was represented within a second major shared subspace of activity in each cortical area. Owing to the redundancy of this representation, decoded tilt remained internally consistent even when it deviated from the actual ground-tilt. Furthermore, persistent homology analysis revealed that the cortical representation of tilt direction was organized into a condition-independent ring topology, which was preserved across cortical subdivisions despite region-specific differences in response properties. Thus, cortical representations of ground-tilt are characterized by a paradoxical coexistence of functional localization and functional sharing: individual cortical areas perform specialized computations while jointly maintaining a coherent tilt manifold that supports a unified representation of the peripersonal environment. We propose that this manifold provides a fundamental body–environment reference frame that enables flexible and adaptive cortical control of behavior.

Introduction

Ground-tilt provides a fundamental body–environment reference frame for stabilizing posture, interpreting sensory inputs and planning actions. The nervous system uses this information across multiple hierarchical levels, ranging from reflex circuits in the brainstem and spinal cord to processing in the cerebellum, basal ganglia, superior colliculus and cerebral cortex [1,2,6]. Among these structures, the cerebral cortex is thought to play a pivotal role in integration across hierarchical levels for postural and movement control [7–11]. Indeed, neurons that encode gravity direction and ground-tilt based on vestibular input have been identified in parietal regions, including primary somatosensory cortex (S1) and posterior parietal cortex (PPC) [12–16]. In rodents, the fronto-parietal cortex, including secondary motor cortex (M2) and PPC, represents body posture [17,18], and postural and movement information is broadly shared across motor and sensory cortices [15,19]. In monkeys, posture-dependent activity related to voluntary movement has been observed in several PPC regions [20]. In addition, during anticipatory postural adjustments, higher motor areas such as M2 and the corticoreticular pathway from the frontal cortex to the reticular formation play central roles, enabling anticipatory responses to ground-tilt through control of proximal musculature [1,6,8–11]. Together, these findings suggest that ground-tilt signals may be computed in parietal and frontal cortices and broadly used as foundational signals for postural and movement control. However, a fundamental question remains regarding cortical representations of ground-tilt. Tilt information must be processed in a specialized manner by particular cortical areas to extract the geometric structure of the environment, yet it must also be shared consistently across multiple cortical areas to support posture control, sensory interpretation and action planning. How such functional localization and functional sharing are reconciled within the cortex remains unclear.

A useful framework for addressing this issue is the concept of low-dimensional subspaces shared across cortical areas. Recent studies have shown that communication between cortical areas is mediated by specific low-dimensional shared subspaces embedded in population activity, termed communication subspaces [21–23]. Activity related to body movement is widely observed throughout the cortex and strongly shapes large-scale cortical dynamics [23–25]. At the same time, cortical activity can covary with internal states such as motivation, salience, arousal and short-term memory [23,24,26–28]. These observations suggest that communication subspaces are strongly influenced by movement-related signals, but may also integrate multiple variables related to body state and the peripersonal environment. If ground-tilt functions as a body–environment reference frame, its cortical representation should appear not only as local selectivity in specific areas, but also as a population manifold shared across the cortex. Thus, understanding cortical representations of ground-tilt requires analysis of both local response properties within individual areas and low-dimensional structures shared across multiple cortical areas. Testing this hypothesis requires precise manipulation of ground-tilt as an external variable, simultaneous monitoring of posture and movement, and large-scale recording of activity across multiple cortical areas.

Here, we developed a new six-degree-of-freedom platform for arbitrary ground motion, termed 6AGM, and combined it with the Diesel2p mesoscope to simultaneously record neural activity across broad dorsal cortical areas and three-dimensional postural kinematics in head-fixed mice during ground-tilt motion [29–31]. By performing experiments in darkness under head-fixed conditions, we minimized visual and vestibular contributions and examined tilt-related activity driven primarily by somatosensory information. We found that ground-tilt was represented

91 locally as tilt selectivity centered on the PPC, while also being represented as a population
92 manifold shared across the dorsal cortex. This shared manifold was preserved across motion
93 conditions and area-specific differences in response properties, providing a common body–
94 environment reference frame through which individual cortical areas can perform specialized
95 computations. Thus, our findings show that cortical representations of ground-tilt are
96 organized through a seemingly paradoxical coexistence of functional localization and
97 functional sharing.
98

Results

Construction and evaluation of the platform

To examine posture and movement and their modulation by ground-tilt, we built a fully open-source platform, 6AGM (**Fig. 1a; Supplementary Video 1,2; Supplementary Information**). The platform was assembled from custom-made components (**Fig. 1b**) and was controlled by four modules (**Extended Data Fig. 1a**). Working sequentially, these modules drove the platform precisely to any specified pose. Motion was generated by six stepper motors located beneath the platform, each of which adjusts the position of a support column along its linear guide. The resulting platform pose was defined by six variables: the 3D center coordinates (X, Y, Z), and the rotation angles (pitch, roll, yaw), which were linked to the actuator positions through the platform's kinematic mapping, f **(Fig. 1c**). To move the platform to a target pose, the control system solved the corresponding inverse kinematic mapping, f^{-1}, determining the required actuator positions. A feedback control mechanism enabled smooth motion (**Fig. 1d; Extended Data Fig. 1b**). To habituate mice to platform motion, we constructed an unstable-board apparatus to habituate head-fixed mice to ground motion (**Extended Data Fig. 1c**). Together, these developments provided a foundation for probing neural responses to ground motion in head-fixed mice.

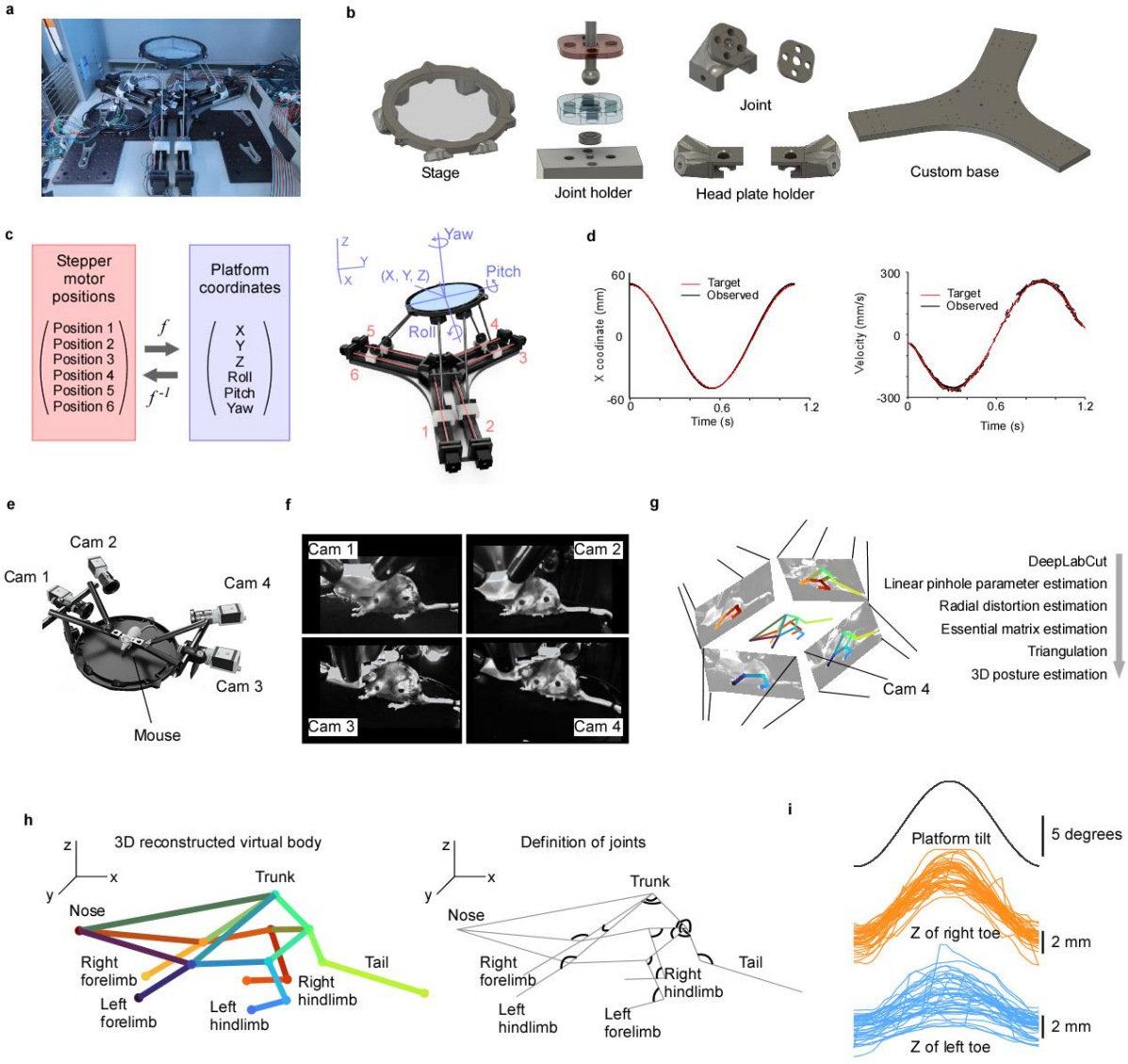


Figure 1 | Development of a new six-degree-of-freedom platform and evaluation of its accuracy

a. Photograph of the new six-degree-of-freedom arbitrary ground motion platform (6AGM).

b. Components of 6AGM (for details, see **Supplementary Information**).

c. The six stepper motors control six pose parameters. The platform pose is defined by the 3D coordinates of the center (X, Y, Z) and the rotation angles (pitch, roll, yaw). A unique mapping, f relates actuator states to platform pose, and the inverse mapping, f^{-1} is used for control.

d. The target position (red) and observed platform position (black) matched accurately in both position and velocity.

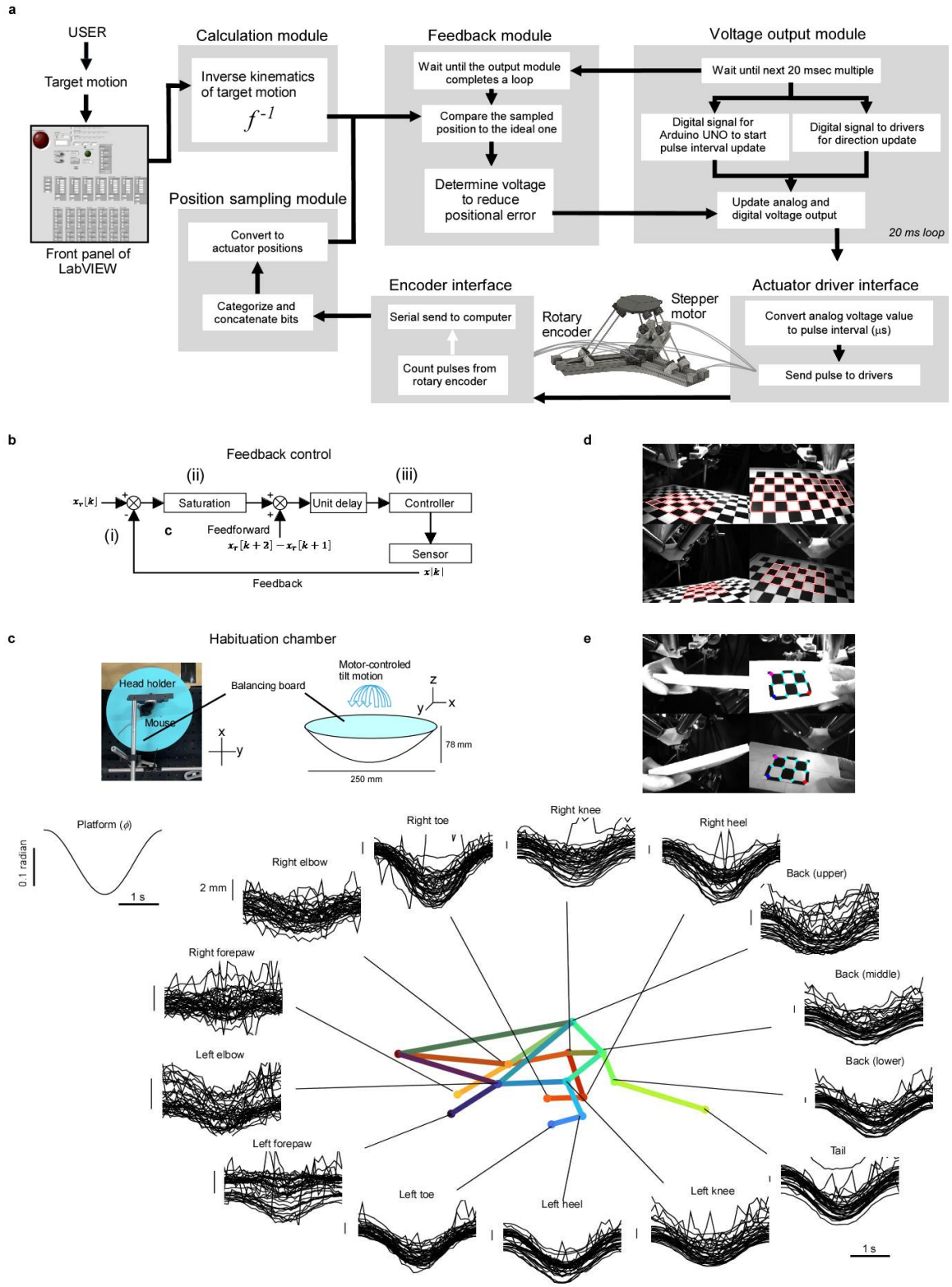
e. Spatial arrangement of the four cameras relative to the platform and the animal.

f. The mouse body imaged simultaneously by four IR-illuminated cameras during two-photon imaging.

g. Images acquired from four cameras were analyzed with DeepLabCut by labeling 15 key points, which were then used for three-dimensional reconstruction. Colors correspond to panel **h**.

h. 3D positions of 15 key points reconstructed from precise multi-camera calibration. We also defined 16 “joints” (right) based on the key points.

i. Changes in the Z coordinates of the left and right hindlimb toe markers while the platform tilts forward and returns. Individual traces show time courses across 40 trials. Data for all 15 key points are shown in **Extended Data Fig. 1f**.



Extended Data Figure 1 | Control design of a six-degree-of-freedom platform and three-dimensional reconstruction of posture.

a. Schematic of platform control. Four modules (Position-Sampling Module, Feedback Module, Calculation Module, Voltage-Output Module) move the platform rapidly and sequentially toward a target pose. The Position sampling module receives precise stepper-motor positions via the encoder interface, and the Voltage output module drives the stepper motors via the actuator driver interface.

b. Schematic of the feedback control. Key features: (i) the current motor positions are read and the error relative to the target pose is computed at each update; (ii) the error is clamped to a maximum value to avoid

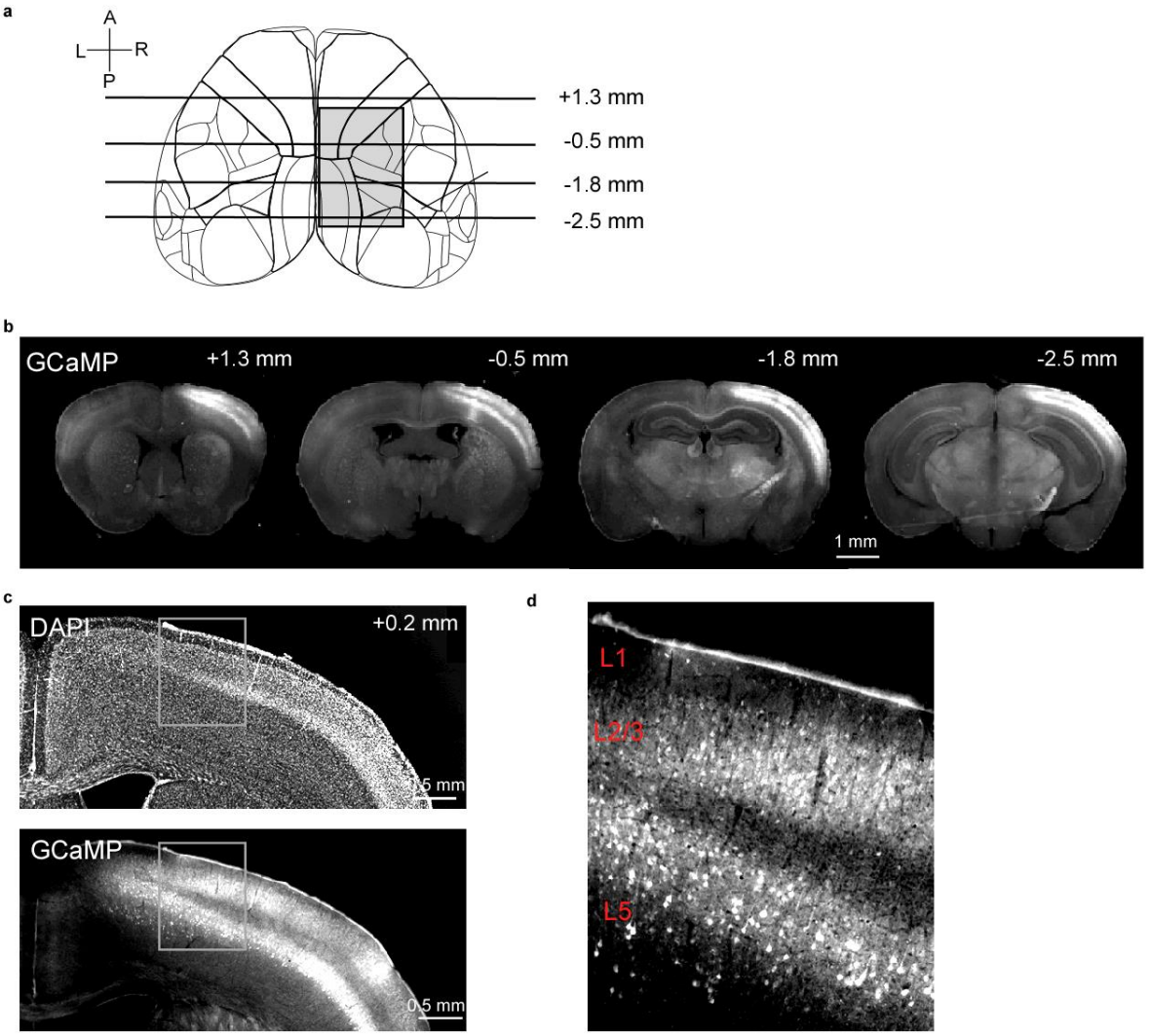
overcompensation; (iii) the combined feedback and feedforward commands yield fast, accurate convergence with minimal overshoot and smooth trajectories.
c. Habituation apparatus. To acclimate mice to ground motion, head-fixed animals were placed on an unstable balance board.
d,e. Examples of checkerboard corner detection for single-camera calibration (**d**) and stereo calibration (**e**). In principle, the images in **e** can also be used for single-camera calibration. However, the smaller checkerboard provides less information about line distortion across the image and is therefore less suitable for estimating radial distortion. By contrast, the larger checkerboard in **d** is more suitable for distortion estimation, but cannot be used for stereo calibration because corresponding points between cameras are not available.
f. Time courses of the Z coordinates of 14 key points over 3 s during forward platform tilt and subsequent return. A total of 40 trials are shown. Vertical bars beside individual traces indicate 2 mm.

Accurate 3D reconstruction of posture

To relate neural activity with posture changes during ground motion, we captured body kinematics with four machine-vision cameras at 290 frames per second (**Fig. 1e,f**). Camera data were processed with DeepLabCut to reconstruct 3D posture (**Fig. 1g,h; Extended Data Fig. 1d,e, Supplementary Video 3**). Accurate multi-camera geometric calibration yielded a spatial accuracy of <0.2 mm. During forward tilts, the Z coordinates of the left and right hindlimb toe markers changed systematically and reproducibly across trials, confirming that platform motion induced consistent vertical displacement of the hindlimbs that was reliably captured by the 3D reconstruction (**Fig. 1i; Extended Data Fig. 1f**). Thus, we successfully induced a range of postures in head-fixed mice while quantifying body posture with high precision.

Identification of sensory areas by one-photon calcium imaging

We used adult mice with broad cortical expression of GCaMP8s following neonatal AAV injection (**Extended Data Fig. 2**), or transgenic mice expressing GCaMP6s. To identify sensory areas, we performed one-photon calcium imaging (**Extended Data Fig. 3a**). In awake, head-fixed mice implanted with a large cranial window, we delivered tactile stimulation to the trunk, tail, and whiskers and identified bilateral S1 subregions (**Extended Data Fig. 3b**). Using these functional maps together with atlas registration, we delineated M1 (primary motor cortex), M2, S1tr (S1 trunk), S1hl (S1 hindlimb), S1fl (S1 forelimb), S1b (S1 barrel), RSC (retrosplenial cortex), and PPC in each mouse (**Extended Data Fig. 3c**).



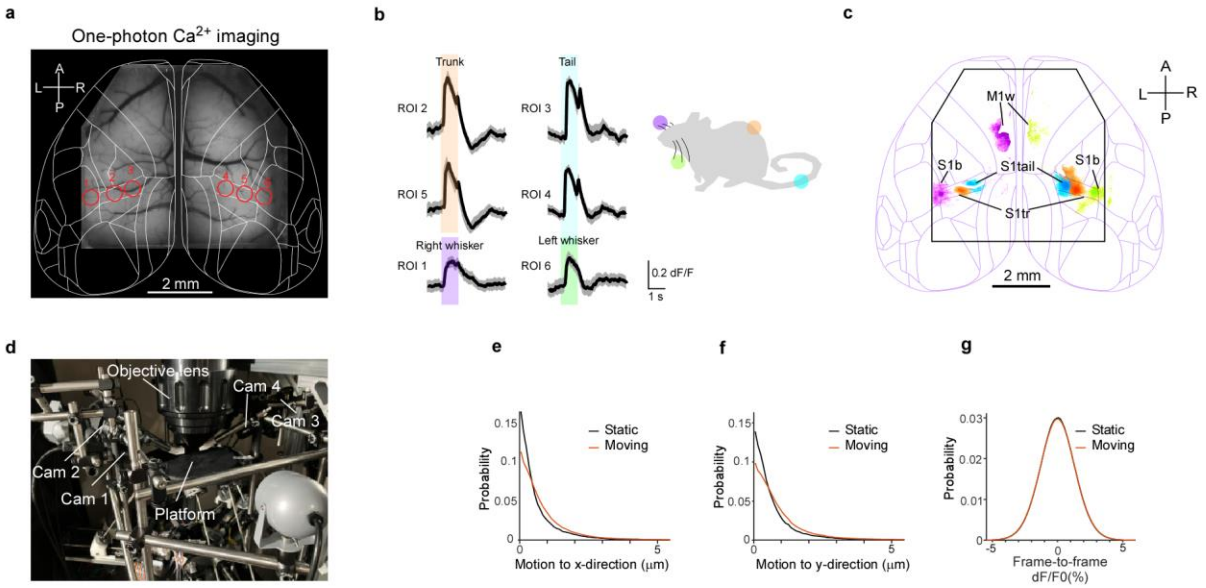
Extended Data Figure 2 | Broad expression of GCaMP8s in mice following AAV injection in pups

a. Dorsal view of the mouse brain. A rectangle indicates a typical two-photon imaging field of view. The horizontal line corresponds to the anterior–posterior (AP) axis position of the coronal section shown below.

b. GCaMP fluorescence image of a coronal section at the AP position indicated in panel a. Numbers denote AP coordinates relative to bregma.

c. DAPI (top) and GCaMP (bottom) images from a coronal section at bregma +0.2 mm.

d. Higher-magnification GCaMP image of the region outlined by the rectangle in panel c. Broad expression of the fluorescent indicator is observed in layers 2/3 and 5.



Extended Data Figure 3 | Functional mapping of sensory cortical areas and estimation of motion artifacts during two-photon imaging under platform movement.

a. Widefield GCaMP fluorescence through a large cranial window with overlays of dorsal cortical areas.

b. Response of ROIs in panel **a** to vibration stimuli delivered to the trunk, tail, and left or right whisker.

c. Cortical responses to vibration stimuli delivered to the trunk (orange), tail (cyan), right whisker (violet), and left whisker (green). S1 subregions for the trunk, tail, and whiskers, as well as whisker-related M1, were clearly mapped.

d. Photograph showing the arrangement of the platform, the objective lens of the two-photon microscope, and the four cameras.

e. X-axis image drift when the platform was static versus moving.

f. Y-axis image drift when the platform was static versus moving.

g. Frame-to-frame fluorescence changes within each ROI during static versus moving periods, computed between adjacent time bins.

Two-photon calcium imaging during platform motion

To broadly survey neural responses to ground-tilt, we moved the platform while performing two-photon calcium imaging with a Diesel2p mesoscope and simultaneously recorded the animal's movements using four cameras at 290 frames per second. We used five motion types, including 8DT (eight-direction tilt) (**Fig. 2a,b; Supplementary Video 3 and 4**). In the 8DT stimulus, the platform tilted by 10° in one of eight directions in a pseudorandom order. The eight directions included forward, backward, left, and right, as well as the four diagonals (front-right, front-left, back-left, back-right). After each tilt, the platform always returned to the default position. Imaging fields measured 3 mm × 4.25 mm and included M2, M1, S1, PPC, and RSC in either the right or left hemisphere (**Fig. 2c**). An example dataset is shown in **Fig. 2d, Extended Data Fig. 4, and Supplementary Video 5**. We recorded a total of 20 sessions from 10 mice, comprising 127,736 active neurons overall and 6,387 ± 452 active neurons per session. Region-wise counts per session were M2: 490 ± 97; M1: 816 ± 54; S1b: 425 ± 72; S1fl: 592 ± 65; S1hl: 648 ± 77; S1tr: 464 ± 52; PPC: 902 ± 94; RSC: 1,168 ± 108; and V1: 309 ± 45; an additional 580 ± 53 neurons per session fell outside the named region contours.

Platform motion does not degrade two-photon image quality

To estimate the impact of platform motion on imaging, we compared X- and Y- axis image drift during moving versus static periods. Drift increased only slightly along both axes during motion

(**Extended Data Fig. 3d-f**). If Z motion was substantial, large frame-to-frame changes in ROI fluorescence would be apparent. We quantified frame-to-frame changes in ROI fluorescence (**Extended Data Fig. 3g**) and found no substantial difference between moving and static periods. Because Z motion in standard calcium imaging tends to produce abrupt downward transients in contrast to the slow decay kinetics of calcium signals, we quantified the incidence of such events as frames in which the change in activity fell below median minus 3 × 1.48 × MAD (median absolute deviation), corresponding to a robust 3-SD threshold. The event rate was 0.30 ± 0.11% during motion and 0.29 ± 0.17% during static periods with negligible difference between conditions. Thus, platform motion had minimal impact on imaging quality.

Identification of tilt direction-selective neurons

We asked whether individual cortical neurons showed selectivity for ground-tilt direction. Examining responses during the 8DT stimulus, we found neurons with sharp tuning to a specific direction (**Fig. 2e**), and found that preferences for backward tilts were most prevalent (**Fig. 2f**). The fraction of direction-selective neurons was significantly higher in S1tr, S1hl, and PPC than in other areas (**Fig. 2g**). Despite regional variation, selective neurons were broadly distributed across the dorsal cortex.

Mapping neurons related to ground-tilt

Because animals adjust posture and generate movements during ground-tilt, selectivity alone cannot isolate neurons specifically encoding ground-tilt from those encoding posture or movement. We therefore applied ridge regression with predictors grouped into posture, movement, and environmental variables (total 1,486) to fit each neuron's activity (**Fig. 2h**; **Extended Data Fig. 5a**). Posture variables comprised 3D coordinates of body parts and joint angles (348 variables in total). Movement variables included velocities, speed magnitudes, accelerations, and acceleration magnitudes of the posture features (1,056 variables in total). Environmental variables comprised tilt direction, tilt angle, and temporal variables aligned to tilt onset (82 variables in total). Notably, by enabling detailed parameterization of whole-body state using high-speed cameras and deep learning-based 3D-posture estimation, this model allowed us to test whether environmental tilt variables explained neural activity beyond a comprehensive, simultaneously measured model of whole-body posture and movement. Although the tilt angle could be predicted from the positions of the distal limbs, analysis of the variance inflation factor (VIF) showed that the tilt-related predictors had VIF values of 2.723 ± 0.308 (Range: 2.259-3.357), indicating little evidence of problematic multicollinearity.

To further assess whether specific body-part-related predictor groups were excessively redundant with the rest of the model, we performed a body-part-specific blockwise VIF analysis. Posture and movement predictors were subdivided into four anatomical chunks: upper limb, lower limb, trunk, and tail. For each chunk, the corresponding predictor block was linearly predicted from all remaining predictors in the full design matrix, and the resulting blockwise R^2 was converted to a VIF. All chunks showed only modest collinearity with the remainder of the model (upper limb, 1.723 ± 0.072, range 1.626 –1.892; lower limb, 1.856 ± 0.060, range 1.748 –1.958; trunk, 1.892 ± 0.073, range 1.773 –2.012; tail, 2.227 ± 0.171, range 1.821 –2.514). Thus, no single body-part-related subspace showed evidence of severe multicollinearity with the rest of the encoding model.

The model successfully predicted the neural activity (**Fig. 2i**). We defined neurons related to posture, movement, or ground-tilt as those within the top 25% of R^2 values, corresponding approximately to $p = 0.0015$, and referred to these neurons as model-explainable neurons

(**MENs; Extended Data Fig. 5b**). Among MENs, comparison of direction selectivity with the sum of absolute ridge coefficients for the tilt-direction parameters revealed a moderate correlation (Pearson's correlation, $r = 0.37$; **Fig. 2j**), indicating that ridge regression successfully extracted direction-selectivity information while mitigating spurious correlations from posture and movement. Because posture, movement, and environmental predictors covaried during behavior, we quantified each contribution using a reduced-model (ablation) approach, measuring the decrease in prediction accuracy (ΔR^2) after excluding each predictor group (**Methods**). We then visualized the spatial distribution of pixel-wise measures computed from neighboring MENs within a 150-μm radius of each pixel, revealing cortical maps of body-part-specific, posture-related, and ground-tilt-related representations. First, somatotopy emerged despite the absence of explicit body-part stimulation in these experiments: maps for forelimb, hindlimb, trunk, and tail were centered on the corresponding S1 subregions (**Fig. 2k**), consistent with the atlas and one-photon sensory maps obtained with vibratory stimulation. We next asked how ground-tilt is represented in the cortex. The local mean decrease in prediction accuracy after ablation of the tilt variables, computed across neighboring MENs, was enriched in the PPC, particularly in RL (rostrolateral) and AM (anteromedial) (**Fig. 2l**). This suggests that the PPC reconstructs tilt information by integrating proprioceptive inputs even in the absence of gravity and vision.

To examine the possibility that the PPC represents patterns of posture rather than tilt information itself, we defined eigenpostures [32,33] by applying principal component analysis to the posture variables (**Fig. 2m**). The top four principal components together explained more than 80% of the total variance, indicating that postural dynamics are largely confined to a low-dimensional subspace. When we mapped the local mean decrease in prediction accuracy across neighboring MENs after separately ablating each eigenposture variable, corresponding to the score of each of the first to fourth principal components, we found that eigenposture-related signals were reflected in many neurons but showed no clear spatial localization (**Fig. 2n**). Therefore, tilt information in the PPC is not simply generated as a reduced representation of body-part information. Rather, the PPC appears to reflect the result of a specific computation that derives tilt information from proprioceptive inputs.

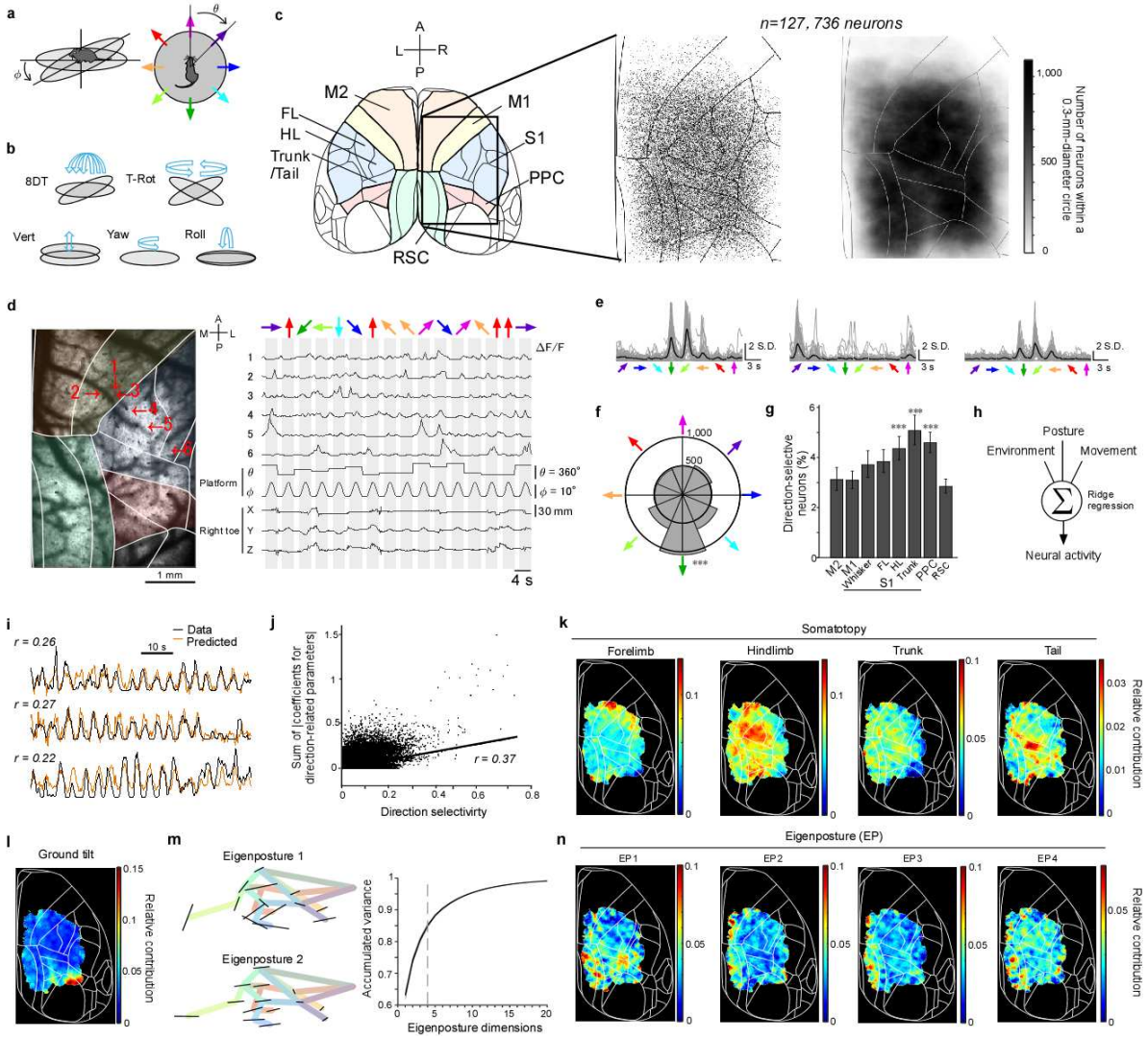


Figure 2 | Distribution across the dorsal cortex of representations related to ground-tilt, movement, and posture

a. Schematic illustration of the two angles, θ and φ, that define the platform tilt.

b. Five types of platform tilt. Abbreviations: 8DT, eight-direction tilt; T-Rot, tilted rotation; Vert, vertical.

c. Left, dorsal view of the mouse cortex and cortical areas. Rectangles indicate approximate two-photon imaging fields. Middle, locations of recorded active neurons (n = 127,736 neurons from 10 mice). Neurons in the left hemisphere were mirror-imaged. Right, density map of these neurons.

d. Mean two-photon GCaMP image (left) with cortical areas overlaid in distinct colors. Right, single-neuron activity traces together with tilt direction (θ), tilt magnitude (φ), and representative body-part kinematics during 8DT. Neuron IDs correspond to the cells marked at left. The complete dataset is shown in **Extended Data Fig. 4.**

e. Direction selectivity of 3 example neurons.

f. Distribution of preferred directions among 4863 direction-selective neurons (χ^2 test, ***$p<10^{-5}$, one-sided binomial test, Bonferroni-corrected).

g. Percentage of direction-selective neurons by cortical area (χ^2 test, ***$p<10^{-3}$, one-sided Fisher's exact vs pooled others, Bonferroni-corrected).

h. Overview of the encoding model. For a detailed description, see Methods and **Extended Data Fig. 5a.**

i. Example neuron: observed activity (black) and ridge-regression prediction (orange).

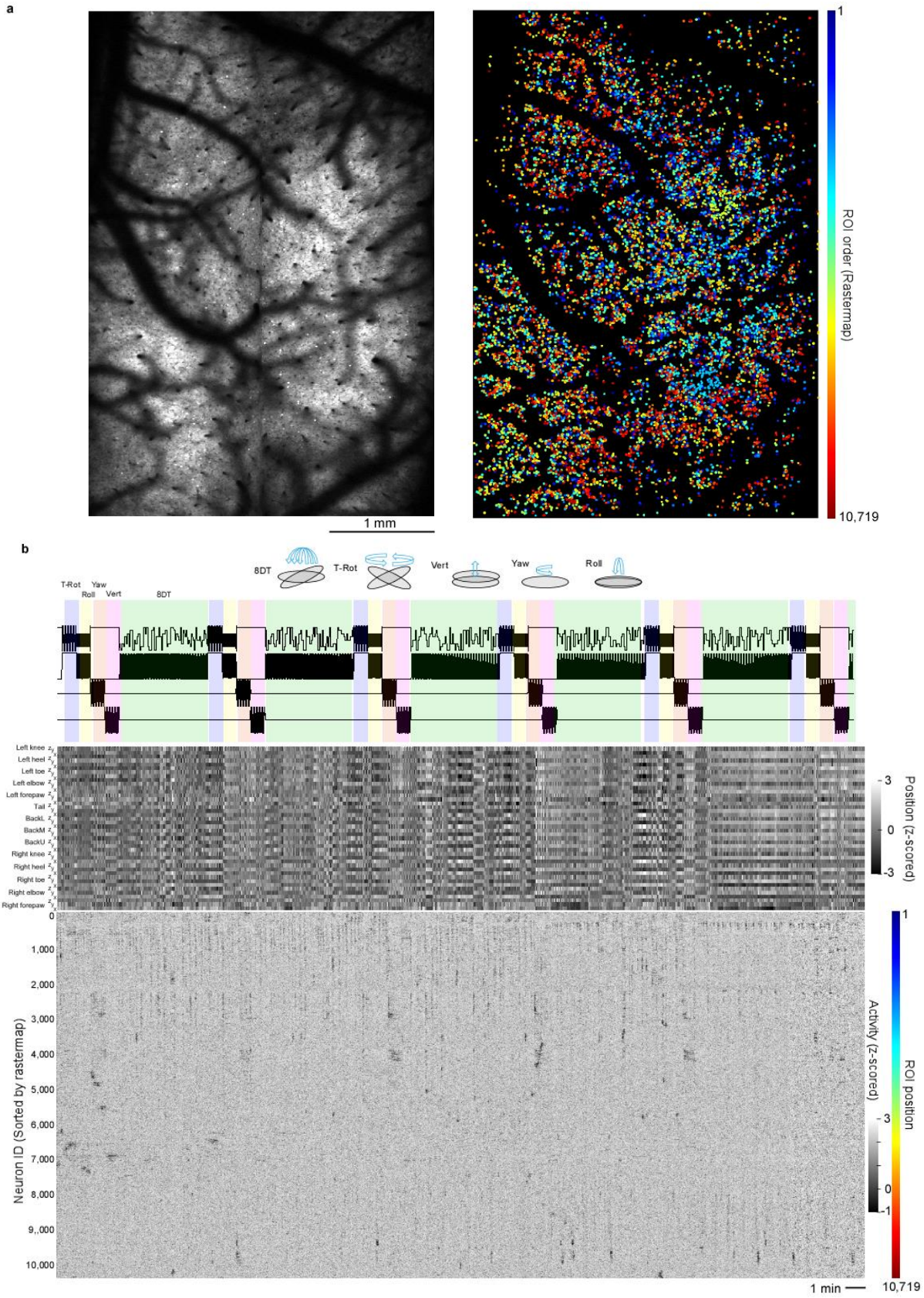
j. Comparison between direction selectivity and the sum of absolute coefficients for direction parameters in the ridge model. A positive correlation was observed (Pearson's correlation r=0.37, $p<10^{-3}$).

k. A map of the relative contribution rates to the encoding model of parameters associated with each body part (forelimb, hindlimb, trunk, tail). Clear somatotopic localization is observed in the forelimb, hindlimb, and tail.

l. A map of the relative contribution rates to the encoding model of parameters related to ground-tilt. Localization is observed in the PPC, particularly in the RL.

m. (left) Examples of eigenpostures 1 and 2 from a representative animal. The black line represents the standard deviation of each individual key point. (Right) The cumulative variance explained by eigenpostures from the 1st to the 20th component (n=20 sessions from 10 mice). The top four components explained more than 80% of the variance.

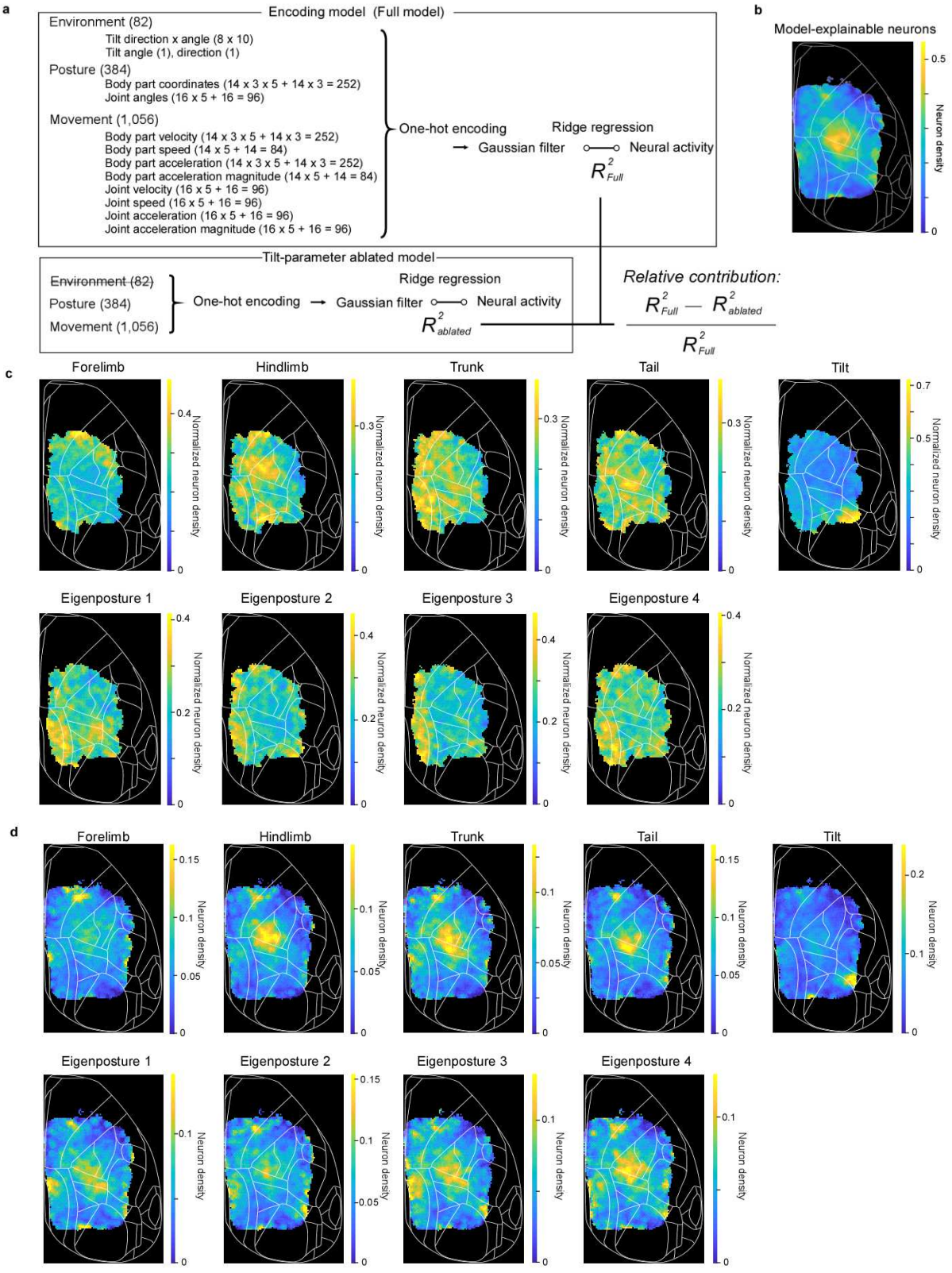
n. A map of the relative contribution rates to the encoding model of parameters related to eigenposture 1–4.



Extended Data Figure 4 | Results of a representative two-photon imaging experiment.

a. Mean image of the two-photon calcium imaging field (left) and ROI locations (right). The colors of the ROIs match the rastermap in panel **b.**

b. Data simultaneously acquired during the two-photon calcium imaging shown in panel **a**. From top to bottom: platform parameters, 3D posture parameters, and neural activity of 10,719 neurons. The neural activity is sorted by rastermap [34].



Extended Data Figure 5 | Encoding model (ridge regression) and maps of neuron density associated with each parameter identified by the model.

a. Parameters used in the encoding model. The number in parentheses indicates the number of parameters. The relative contribution of each parameter was calculated by comparing the R^2 of the full model with that of an ablated model in which the corresponding parameter group was excluded. In this example, tilt-related parameters were ablated.

b. Density distribution of the top 25% of neurons with high R^2 values in the full encoding model, referred to as MENs. The 75th percentile R^2 value corresponded to a statistical significance of $p = 0.0015$.

c. Density distribution of MENs in the top 25% of relative contribution for each parameter. The 75th percentile of relative contribution corresponded to $p = 0.034$ for forelimb, $p = 0.019$ for hindlimb, $p = 0.026$ for trunk, $p = 0.116$ for tail, $p = 0.014$ for tilt, $p = 0.037$ for Eigenposture 1, $p = 0.046$ for Eigenposture 2, $p = 0.042$ for Eigenposture 3, and $p = 0.055$ for Eigenposture 4.

d. Density distribution of neurons, with those in the top 25% of relative contribution for each parameter, relative to all neurons.

The analyses described above were restricted to MENs, which were abundant in S1tr and S1hl. In contrast, when we extended the analysis to all active neurons, rather than only MENs, and examined the density of neurons related to each parameter, we found that, for all variables, neurons related to each parameter were enriched in S1tr and S1hl, where MEN density was high (**Extended Data Fig. 5c,d**). These results indicate that, although clear functional localization was present, S1tr and S1hl contained many neurons related to diverse aspects of the experimental environment.

Ground-tilt can be decoded from neural activity across the dorsal cortex

So far, we have characterized the cortical distribution of neurons related to body parts, tilt, and posture. However, population-level representations may rely on complementary tuning across neurons and thus cannot be fully captured by single-neuron analyses alone. To directly assess tilt information at the population level, we decoded tilt direction from a population of 200 randomly selected neurons within each cortical area during 8DT, T-Rot, and Roll conditions (**Fig. 3a-c**). Across three conditions, decoding performance was highest in S1tr and S1hl and PPC showed relatively high performance. However, the localization was modest; even in areas with lower average performance such as M2, M1, and RSC, the scores were at least 60% of those in S1tr, S1hl, and PPC. These results indicate that, insofar as the information was decodable, regions across the dorsal cortex beyond PPC also represented ground-tilt information, whether directly or indirectly. A similarly widespread pattern of representation was also observed for yaw and vertical translation (**Fig. 3d,e**). Thus, whereas single-neuron and encoding analyses revealed local enrichment of tilt-related signals in the PPC, population decoding showed that tilt information was accessible across the dorsal cortex.

Functional coordination of tilt information across cortical regions

This apparent contrast between local enrichment and widespread decodability led us to ask whether tilt information is represented as a shared population-level structure across cortical areas. To address this question, we first divided the neural population into neurons from the parietal cortex (S1 and PPC) and neurons from the frontal cortex (M1 and M2). Decoding using the parietal cortex alone achieved higher mutual information than decoding using the frontal cortex (parietal: 0.23 bits; frontal: 0.087 bits; **Fig. 3f,g**) consistent with the area-level decoding performance described above. To examine the coordination between the frontal and parietal cortices, we plotted a histogram of the difference in decoding offsets between the two regions.

The offset was defined as the difference between the true direction and the decoded direction. The offset differences were significantly concentrated around zero, indicating coordinated representation of tilt direction (**Fig. 3h**). Furthermore, the joint distribution of decoding offsets in the frontal and parietal cortices showed that the diagonal elements, representing agreement between the two regions, were significantly higher than expected under independence (the product of the marginals) (**Fig. 3i**). This indicates that even when both the frontal and parietal cortices produced errors, their representations nevertheless remained coordinated. Together, these results suggest that tilt information distributed across the dorsal cortex is not simply redundant but instead contributes to an internally consistent ground-tilt representation through functional coordination.

Broadcast subspace analysis using GCARP reveals the information content of shared dynamics

Although tilt information was found to be widely shared across the dorsal cortex, an important question is whether tilt information occupies a dominant position among the information shared across dorsal cortical areas. To address this question, we extended the communication subspace framework for inter-areal shared subspaces [21] and defined a broadcast subspace. Specifically, we employed generalized canonical correlation analysis (GCCA), which generalizes CCA from pairs of areas to multiple areas. GCCA applies a linear transformation to the population activity of each area and extracts latent time series that are maximally correlated across all transformed series (**Fig. 3j**). These latent time series are ordered according to the amount of variance shared across areas. We then quantified the information content of each GCCA component using GCARP (generalized canonical component ablation-based representational probing), an extension of our recently developed CARP framework [23]. In GCARP, we first decoded target variables from the full set of GCCA component time series, which represent the common dynamics expressed across all recorded areas. Decoding based on them therefore captures information jointly represented across areas. We then ablated one component and repeated decoding with the remaining components. The reduction in decoding performance quantifies the contribution of the removed component to the target variable, thereby revealing which shared components across areas carry which types of information (**Fig. 3k**).

In the 8DT session, we applied GCARP to neural activity recorded from eight areas (M2, M1, S1b, S1hl, S1fl, S1tr, PPC, and RSC) and evaluated three types of information: movement, ground-tilt, and the first eigenposture. The significant axes were the 1st GCCA component for movement, and the 1st–3rd GCCA components for tilt and posture. Interestingly, movement was most strongly represented in the first GCCA component, whereas ground-tilt was most strongly represented in the second, and posture was also significantly represented in the third (**Fig. 3l**). Thus, the dynamics shared across broad regions of the dorsal cortex reflect movement, tilt, and posture.

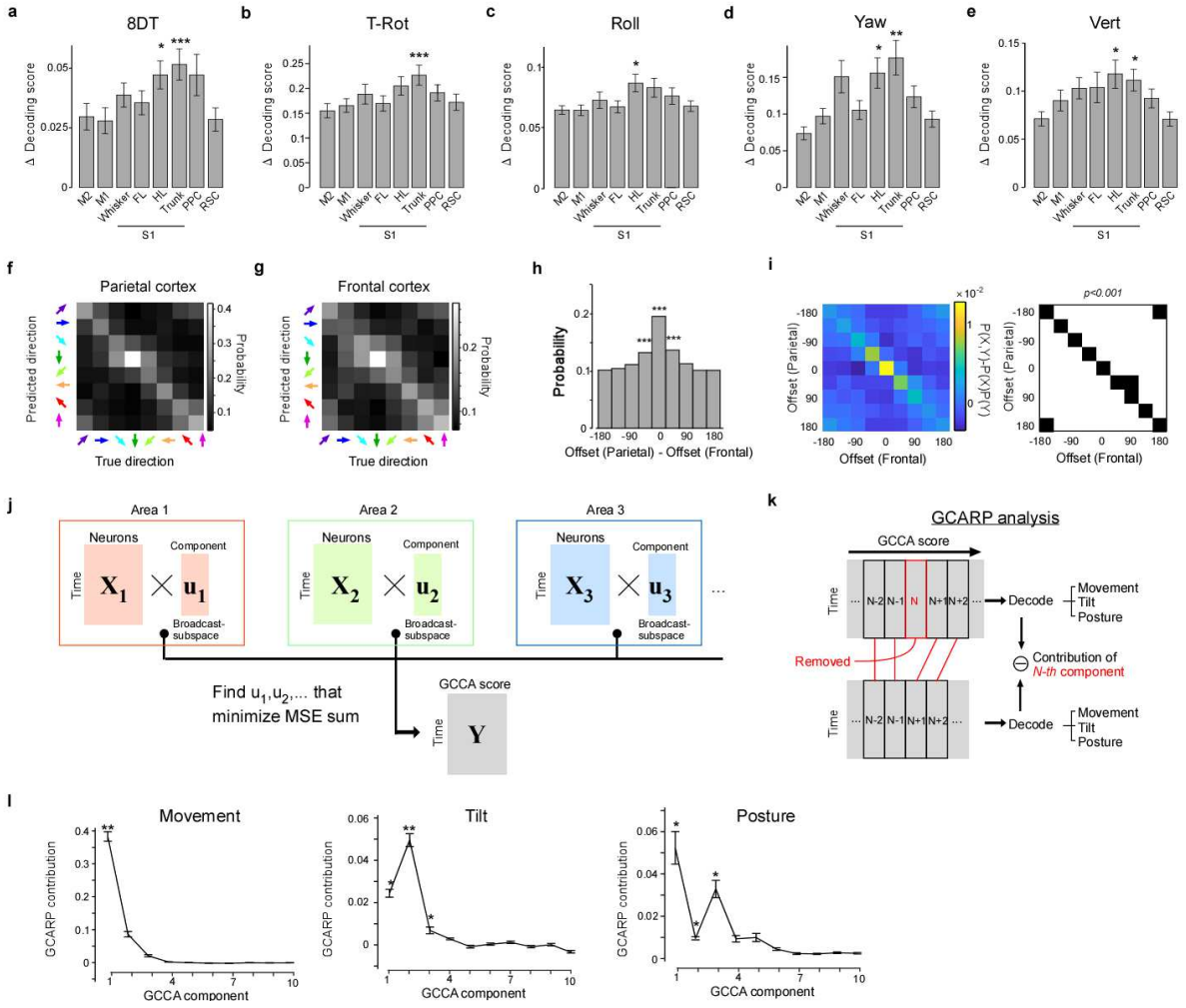


Figure 3 | Distributed and coordinated representations of ground-tilt in the dorsal cortex revealed by decoding and GCARP analysis

a-e. Decoding analysis. From each cortical area, 200 neurons were randomly sampled for decoding. For 8DT (**a**) and T-Rot (**b**) sessions, performance was defined as the probability that the decoded tilt direction was within 45° of the true direction. For Roll (**c**), Yaw (**d**), and Vert (**e**) sessions, performance was the R^2 of the decoded parameter (**Methods**). In all cases, the Δscore was computed as the difference between the observed score and the mean score from randomly shuffled data. Across all motion types, Δscores for S1tr and S1hl exceeded those of other areas (*p<0.05; **p<0.01; ***$p<10^{-3}$; one-vs-rest, Wilcoxon's rank-sum test, Bonferroni corrected).

f. Confusion matrix of tilt-direction decoding during the 8DT session using neurons in the parietal cortex (S1 and PPC).

g. Same analysis as in **f**, using neurons in the frontal cortex (M1 and M2).

h. Histogram of the difference between decoded angles from frontal versus parietal cortex (based on the decoding results in **f** and **g**). The zero bin was significantly overrepresented (***$p<10^{-3}$; Binomial test, Bonferroni corrected).

i. Left, the joint distribution of decoding results from the frontal and parietal cortices after subtracting the distribution expected under independence (product of the marginals). Right, bins with significantly elevated probability are shown in black ($p<10^{-3}$; Binomial test with Bonferroni correction).

j. Schematic of GCCA (generalized canonical correlation analysis).

k. Schematic of GCARP (generalized canonical component ablation-based representational probing).

l. GCARP results showing shared dynamics aligned with movement (left), ground-tilt (middle), and posture (eigenposture 1, right) (*p<0.05, **p $<10^{-3}$; Wilcoxon's signed-rank test, Bonferroni corrected).

Universality of the tilt-space

We next shifted our focus from the distribution of tilt information to the format of its representation. First, we examined whether tilt-related neurons represent tilt direction invariantly across motion types. In other words, do they represent tilt direction independently of the specific motion trajectory? To address this, we compared single-neuron responses between the 8DT and T-Rot stimuli. In three representative neurons, the preferred directions identified during 8DT were consistent with those measured under T-Rot (**Fig. 4a**). The activity of direction-selective neurons aligned to the tilt phase showed strong correlations between 8DT and T-Rot (**Fig. 4b**). These findings indicate that ground-tilt is encoded in a common format across motion types, invariant to the type of platform motion.

We next asked how populations of neurons organize tilt information. One possibility is that, analogous to head direction cells [35], these neurons collectively form a low-dimensional circular manifold. To address this question, we investigated whether a neural manifold specific to ground-tilt existed. Using cPCA (**Fig. 4c**), we maximized the following objective:

$$\Sigma = (1-w)[within-trial\ variance] - w\,[across-trial\ variance].$$

where w is a scalar constant ranging from 0 to 1. This method extracts axes that exhibit large within-trial variance but small across-trial variance, thereby capturing dominant activities that are consistent across trials. The cPCA analysis applied to the 8DT data revealed that activity during the 8DT traced trajectories that preserved the stimulus topology, with smooth transitions among the eight directions (**Fig. 4d; Supplementary Video 6**). When the same axes were used to visualize responses during T-Rot, trajectories formed a circular orbit parameterized by the instantaneous tilt angle (**Fig. 4e**). Importantly, these axes were obtained from the 8DT data, not from the T-Rot data. Similar projections during Roll sessions aligned with the lateral tilt dimension identified in the 8DT trajectory (**Fig. 4f**). These results suggest that a "tilt-space" is embedded in dorsal cortical population activity and is expressed in a common format across ground motion patterns.

We then projected activity during Vert and Yaw onto the cPCA space derived from 8DT (**Fig. 4g, h**). Intriguingly, Vert also produced a circular trajectory, implying that this space is not exclusively tilt-specific. In contrast, Yaw did not yield a ring structure. Thus, the cPCA space derived from the 8DT captures tilt-space but also partially incorporates non-tilt components.

Distilling the tilt-space using gcPCA

To suppress the Vert component and isolate a more tilt-selective subspace, we extended cPCA and revised the objective (**Fig. 4i; Methods**):

$$\begin{aligned}\Sigma = {} & (1-w_1)[within-trial\ variance\ during\ 8DT] \\ & - w_1\,[across-trial\ variance\ during\ 8DT] \\ & - w_2\,[within-trial\ variance\ during\ Vert].\end{aligned}$$

We refer to this as generalized cPCA (**gcPCA**). We visualized trajectories for all five stimulus types in the top three gcPCA dimensions (**Fig. 4j-n**). The ring structure associated with Vert disappeared, whereas the ring structures for 8DT, T-Rot, and Roll were preserved. Thus, gcPCA demonstrated a more selective neural subspace for tilt representation.

To examine whether this common ring-topology is preserved across animals and sessions, we evaluated ellipses in a lower-dimensional space. We applied gcPCA using T-Rot as condition 1 and Vert as condition 2, and projected the data onto the leading two-dimensional plane. At $w_2 = 0$, ellipses were observed for T-Rot, Vert, and 8DT (**Fig. 4o**). As w_2 increased, the ellipse for Vert progressively shrank. When quantified by ellipse area, the reductions in area for T-Rot and 8DT were significantly smaller than the reduction for Vert (**Fig. 4p**). Notably,

the axis ratios of these ellipses decreased significantly with increasing w_2, indicating that removal of Vert-related activity led to the extraction of a more uniform tilt-space (**Fig. 4q**). Thus, gcPCA successfully isolated tilt-space from neural activity in the dorsal cortex.

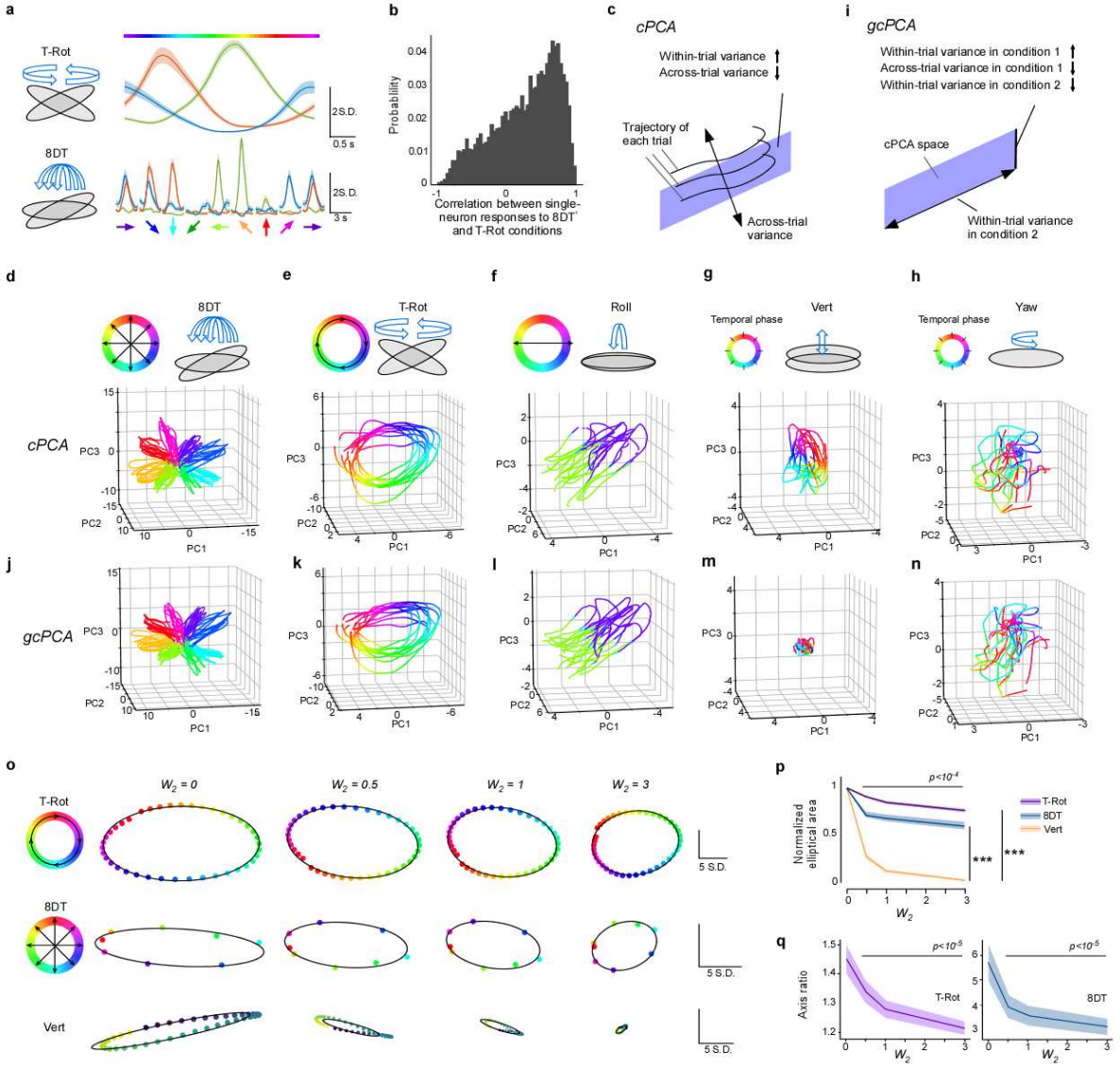


Figure 4 | Identification of a universal representational space for tilt direction

a. Example activity from three neurons during T-Rot (top) and the responses of the same neurons during the 8DT stimulus (bottom). Direction-selective activity was preserved across the two paradigms.

b. Correlation coefficients between phase-selective responses to T-Rot and 8DT in individual direction-selective neurons.

c. Contrastive PCA (cPCA) defines axes that maximize within-trial variance while minimizing across-trial variance for population activity. The trade-off between these two terms is controlled by a parameter w.

d. cPCA applied to responses during the 8DT stimulus. Population activity that mirrors tilt direction appears in the top three cPCA dimensions. Trajectories were computed from trial-averaged activity across five trials. Color denotes tilt direction.

e. The same neuronal population, projected onto the same cPCA axes as in **d**, but plotted for activity during T-Rot. Color denotes instantaneous tilt direction. Note that the rotation topology is preserved using axes derived from the 8DT condition rather than from the T-Rot data.

f-h. The same population and cPCA axes, plotted for a Roll session (**f**), a Vert session (**g**), and a Yaw session (**h**).

i. Generalized cPCA (gcPCA) extends cPCA to identify axes with large within-trial variance in condition 1, small across-trial variance for condition 1, and reduced within-trial variance for condition 2. The trade-off is controlled by parameters w_1 and w_2.
j–n. Trajectories for each stimulus type projected onto the top three gcPCA dimensions. Each of **j–n** corresponds to the panels shown in **d–h**.
o. Representative trajectories after dimensionality reduction to two dimensions by gcPCA. w_1 was fixed at 0.5, and four values of w_2 (0, 0.5, 1, and 3) were tested. The top, middle, and bottom rows correspond to T-Rot, 8DT, and Vert stimuli, respectively. When $w_2 = 0$ (equivalent to cPCA), ellipses were observed not only for T-Rot and 8DT but also for Vert. As w_2 increased, the ellipse for Vert became smaller, whereas those for T-Rot and 8DT showed little change.
p. Normalized ellipse area as a function of w_2, with w_1 fixed at 0.5 (n = 20 sessions from 10 mice). In all cases, the ellipse areas with $w_2 > 0$ were significantly smaller than those with $w_2 = 0$ ($p<10^{-4}$; Wilcoxon's signed-rank test). The slope for Vert was significantly more negative than that for T-Rot or 8DT (***$p<10^{-4}$; one-sided Wilcoxon's signed-rank test on per-plane log-area slopes, Bonferroni-corrected).
q. Same analysis as in **p**, but for the ellipse axis ratio ($p<10^{-5}$; Wilcoxon's signed-rank test).

Topological invariance of the tilt-space in high-dimensional neural activity

Ellipse-based analyses require identifying the two-dimensional subspace in which the elliptical structure is observed, but it remains unclear whether the tilt-space exhibits a ring topology in higher-dimensional representations. To address this question, we performed a persistent homology analysis [36]. In persistent homology, ring-like topological features are detected by progressively expanding spheres centered at each data point in the neural activity space (**Fig. 5a**). We reduced the T-Rot data to five dimensions using gcPCA and analyzed the ring topology in this five-dimensional space by focusing on the first homology group (H_1). T-Rot exhibited H_1 cycles with long lifetimes across all values of w_2, whereas H_1 lifetimes in Vert decreased as w_2 increased (**Fig. 5b–d**). The 8DT condition showed a trend similar to that of T-Rot. Together, these results indicate that the ring topology observed in T-Rot persists in higher dimensions independently of the topology present in Vert, thereby supporting the validity of ellipse-based analyses in higher-dimensional tilt-space representations.

To quantify the dominance of the ring topology, we introduced the Landscape Ringness Index (LRI), derived from the H_1 persistence landscape [37] (**Fig. 5e**). The LRI measures how strongly the topological signal is concentrated in a single dominant H_1 cycle relative to other H_1 cycles. In the ideal case of points perfectly arranged on a circle, the LRI equals 1, reflecting that nearly all landscape mass resides in the first layer. When one coherent H_1 cycle dominates and other cycles are relatively weak, the LRI approaches 1. In contrast, it decreases toward 0 when multiple cycles of comparable strength coexist, indicating fragmentation of the ring topology. Importantly, because the LRI is defined as a ratio of landscape integrals, it is invariant to global rescaling of the embedding and therefore does not decrease simply due to reduced overall dispersion. The LRI was high for T-Rot and 8DT across all values of w_2, whereas it remained significantly lower for Vert throughout the entire w_2 range (**Fig. 5f**). This indicates that T-Rot and 8DT contain a single dominant H_1 cycle in high-dimensional space, whereas the topology of Vert in higher dimensions is not dominated by a single coherent H_1 cycle but instead is distributed across multiple competing H_1 cycles. These results demonstrate that the dominant elliptical structure visualized in the two-dimensional tilt-space projection for T-Rot and 8DT reflects intrinsic population topology rather than variance magnitude or projection artifacts, thereby supporting the invariance of the tilt-space representation.

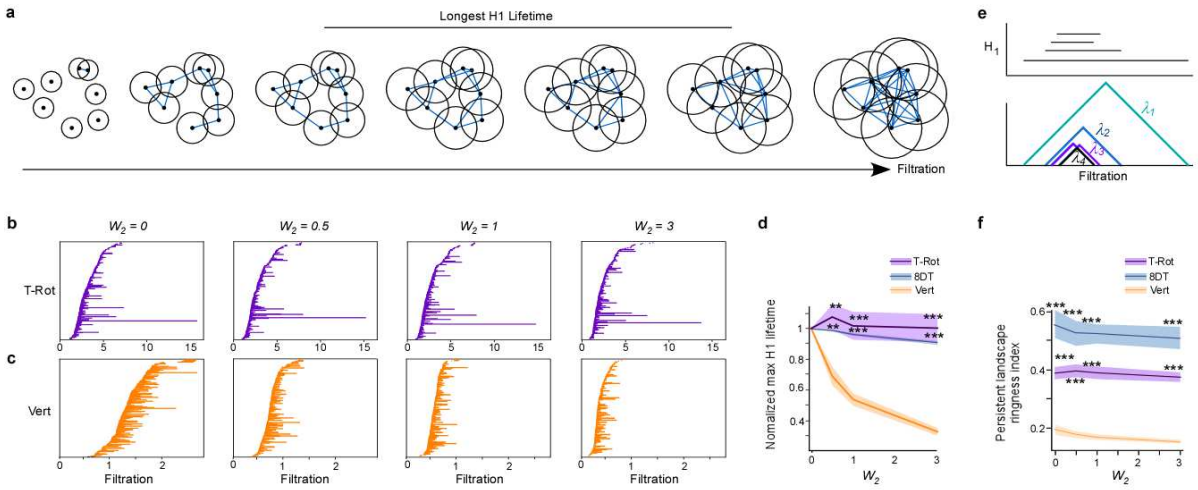


Figure 5 | Persistent homology analysis

a. As the filtration scale increases, expanding balls around data points form a simplicial complex, giving rise to loops (H1) that are created (birth) and later merge or disappear (death). The lifetime of each loop is defined by the difference between its birth and death scales. In this case, H1 component with the longest lifetime corresponds to the most prominent loop structure in the data. The rightward arrow indicates filtration progression.

b. Barcode plots of all H1 components for neural activity during T-Rot shown for different values of w_2.

c. Barcode plots of all H1 components for neural activity during Vert shown for different values of w_2.

d. Comparison of the maximum H1 lifetime across conditions. Values were normalized to the condition with w_2 = 0. (**p<10^{-2}, ***p<10^{-3}; Wilcoxon's signed-rank test of log max H1 lifetime vs Vert).

e. The top panel shows a barcode representation of first homology (H1) components across the filtration. The bottom panel illustrates the construction of the persistent landscape, in which each H1 interval is mapped to a tent function defined by its birth and death values. The persistent landscape is given by a sequence of envelope functions (λ_1, λ_2, …), with λ_1 representing the most persistent topological feature at each filtration value. The ringness index is calculated based on these envelope functions (see Methods for details).

f. Comparison of the persistence LRI across conditions. (***p<10^{-3}; Wilcoxon's signed-rank test vs Vert).

A universal ring-topological format is shared across the dorsal cortical areas

We have shown that tilt information is widely shared across the cortex and that it is represented in a common ring-topological format. We next asked whether this ring-topological format is preserved across distributed cortical areas. If the invariant tilt-space reflects a broadly shared cortical representation, similar manifold structures should be recoverable from major cortical subdivisions. To test this possibility, we repeated gcPCA in three neuronal subsets: PPC, S1, and the remaining areas, including M1, M2, and RSC (**Fig. 6a**). In each case, neural population trajectories preserved the topology of the stimulus: during 8DT, activity transitioned smoothly among tilt directions, and during T-Rot, it formed a circular trajectory parameterized by tilt angle. To quantify the stability of these structures, we computed the LRI for tilt-spaces obtained from each subdivision. Across sessions, LRI values remained high and comparable to those obtained from the full neuronal population **(Fig. 6b)**, indicating that the ring topology of the tilt-space is preserved even when the analysis is restricted to specific cortical subdivisions. Thus, the invariant tilt manifold is not confined to a single cortical region but is broadly distributed across the dorsal cortex.

Relationship between tilt-space and shared cortical dynamics

Finally, to directly examine the relationship between the shared dynamics and the tilt-space, we projected the 1st–10th GCCA components onto the top three or top five dimensions of

gcPCA and evaluated the fraction of squared magnitude of each GCCA axis captured by the gcPCA subspace. The strongest alignment was observed for the second GCCA component, which GCARP identified as encoding tilt information (**Fig. 6c**). Although the first component also exhibited a substantial projection onto this subspace, the remaining shared components showed much weaker projections onto the tilt-space. These results indicate that tilt-related dynamics are prominently embedded within the broadcast subspace shared across cortical areas and align strongly with the invariant tilt-space identified by gcPCA.

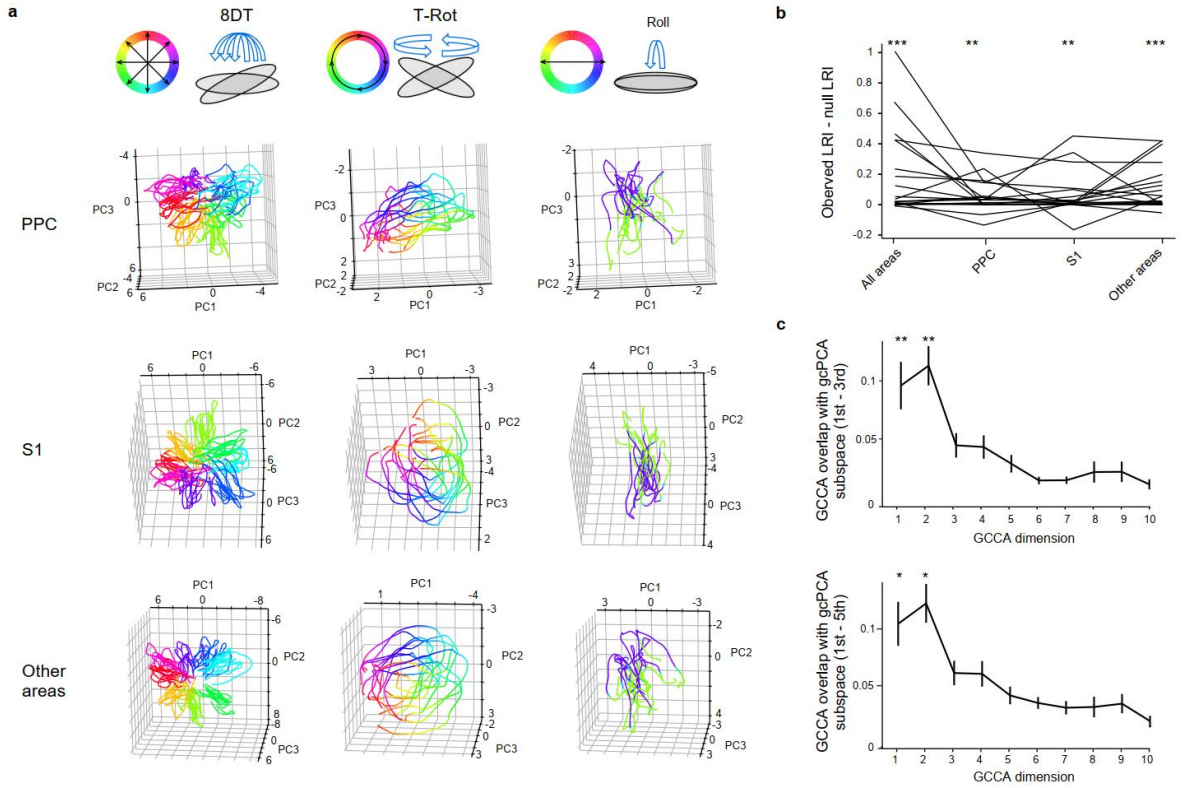


Figure 6 | Tilt-space forms a shared manifold across the dorsal cortex

a. gcPCA population trajectories computed from neurons in different cortical subdivisions. gcPCA was performed separately using neurons from PPC, S1, and the other areas. Trajectories were computed from trial-averaged activity across five trials and are shown for the 8DT (left), T-Rot (middle), and T-Rot stimuli (right).

b. Comparison of the LRI subtracted from null LRI obtained from gcPCA with neurons in different cortical subdivision. Null LRI was obtained through standard PCA (n = 20 sessions from 10 mice). (**p<0.01, ***p $<10^{-3}$; Wilcoxon's signed-rank test against zero, Bonferroni corrected).

c. Fraction of each GCCA axis captured by the gcPCA subspace (top: 1st – 3rd dimensions; bottom: 1st – 5th dimensions). The top three and top five dimensions correspond to those used for trajectory visualization (panel **a**) and for the LRI analysis (panel **b**), respectively. (*p<0.05, **p $<10^{-3}$; Wilcoxon's signed-rank test vs. the median of the other data, Bonferroni corrected).

Discussion

By combining a newly developed six-degree-of-freedom platform (6AGM) for head-fixed mice with a Diesel2p mesoscope, we simultaneously imaged neural activity across dorsal cortical areas, including M1, M2, S1tr, S1hl, S1fl, S1b, PPC, and RSC, together with three-dimensional postural kinematics at high spatiotemporal resolution during ground-tilt motions. Analyses of neurons related to posture and environmental tilt revealed four main findings. First, neurons in the dorsal cortex exhibited sharp selectivity for tilt direction. Second, these direction-selective neurons were broadly distributed but enriched in the PPC. Third, broadcast subspace analysis showed that movement, tilt and posture information were represented in the leading shared dimensions, and that the population code for tilt remained self-consistent across the fronto-parietal cortex. Fourth, population activity formed a tilt-space with a ring topology that was preserved across motion conditions and shared across cortical areas. Together, these results show that cortical representations of environmental tilt are characterized by a paradoxical coexistence of functional localization centered on the PPC and a shared manifold distributed across the dorsal cortex. This organization may allow individual cortical areas to perform specialized local computations while sharing a common body–environment reference frame.

The enrichment of tilt-selective neurons in the PPC suggests that this area acts as a local computational hub that integrates multi-joint proprioceptive inputs and extracts the geometric structure of the environment. In this study, the information available for estimating tilt did not include visual or vestibular gravitational cues; rather, ground-tilt was likely inferred from proprioceptive signals arising from multiple body parts [38]. In contrast, neurons associated with eigenpostures were not confined to the PPC or S1, but were broadly distributed across the cortex. Thus, the tilt representation centered on the PPC is unlikely to be a mere reflection of posture statistics, but instead appears to reflect an active representation of environmental tilt. However, this enrichment in the PPC does not mean that tilt representation is confined to the PPC. Rather, the PPC may serve as a specialized hub for extracting tilt information, while this representation is shared across dorsal cortical areas at the population level. Indeed, tilt-selective activity across broad cortical regions, including the PPC, maintained consistent preferred angles across different motion conditions, and rotational trajectories formed a continuous ring in gcPCA space. We therefore propose that tilt information is represented in a universal coordinate system that is preserved across changes in posture and movement, linking local functional specialization with cortex-wide functional sharing.

To investigate population dynamics broadly shared across the cortex, we developed GCARP. GCARP revealed that the first component of the broadcast subspace primarily captured movement-related variables, whereas the tilt-space aligned most strongly with the second component. The identification of the first component as a “movement axis” is consistent with our previous findings [23] as well as with prior studies [32,33]. Shared posture information was also prominently represented in the third component. Together, these results indicate that the broadcast subspace represents dynamic body information, static body information and information about the peripersonal environment in an integrated yet partially separable manner. Importantly, in contrast to the enrichment of tilt-selective neurons in the PPC, the tilt-space emerged as a second major population dimension that was broadly shared across the dorsal cortex. This organization may allow individual cortical areas to perform distinct local computations while referring to a common tilt coordinate system. Thus, a key function of the

broadcast subspace may be to link functionally specialized cortical areas into a self-consistent body–environment representation.

The continuous phase representation of tilt suggests that the tilt-space variable may be supported by attractor-like population dynamics, analogous to those described for head-direction cells [39]. Similar attractor dynamics have also been reported in place cells [40,41] and grid cells [42]. The ring topology identified in this study was preserved across motion conditions and cortical subdivisions, despite differences in local response properties. This preservation suggests that the essential structure of cortical tilt representation lies not only in the tuning of individual neurons or the response strength of specific cortical areas, but also in a shared population manifold distributed across cortical regions. Moreover, such a redundant and conserved manifold may provide a basis for maintaining internal consistency of the representation even when the decoded tilt deviates from the actual ground-tilt. A universal coordinate system for tilt would be particularly useful if the continuous phase representation of tilt interacts with networks that represent place and orientation. Indeed, our results suggest that the dorsal cortex itself shares this coordinate system for tilt. How the representation of the peripersonal environment in the dorsal cortex relates to broader spatial representations in temporal lobe networks will be an important question for future study.

Our fully open-source six-degree-of-freedom platform (6AGM) provides the stability required for two-photon imaging while allowing arbitrary translations and rotations. Mounting a treadmill on the platform would enable navigation experiments on slopes. Compared with floating balls [43], rotating disks [44], or wheels [45], this setup substantially expands the degrees of freedom for navigation paradigms. Coupling the system to a head-rotation module [46] may further allow free exploration of two-dimensional environments with slopes. Applying this platform to neurological disease models with postural instability may facilitate pathophysiological research, therapeutic development, and rehabilitation. Thus, this platform provides foundational infrastructure with broad applications, ranging from basic neuroscience to clinical neurology.

Methods

Animal preparation

All experiments were approved by the Animal Research Ethics Committee of the Institutional Animal Care and Use Committee of the Institute of Science Tokyo (A2021-290C6, A2024-060C2) and were carried out in accordance with the Fundamental Guidelines for Proper Conduct of Animal Experiment and Related Activities in Academic Research Institutions (Ministry of Education, Culture, Sports, Science and Technology of Japan). Two double-transgenic adult mice (one female and one male) expressing GCaMP6s and eight adult C57BL/6Jcl mice (two female and six male) expressing GCaMP8s through neonatal AAV (adeno-associated virus) injection were used. Double-transgenic mice (C57BL/6Jcl) were generated by crossing the Vglut1-Cre mice and Ai162 mice [47] that can express GCaMP6s in excitatory neurons in a Cre-dependent manner. Doxycycline was administered to double transgenic mice during development to suppress transgene expression and mitigate potential developmental effects of calcium buffering. Mice were kept under an inverted light schedule (lights off at 12 AM; lights on at 12 PM) in their home cages to adapt them to the experimental environments.

Neonatal AAV injection

Eight mice in the study underwent neonatal virus injection on postnatal day 1 or 2 [23,48]. The pups were placed on an ice bed for anesthesia. A custom head-fixation device developed by the NARISHIGE group was used to fix the pup's head. A borosilicate glass pipette with an outer diameter of 50 μm and inner diameter of 30 μm was inserted into the head 250–300 μm deep from the surface. Four μl of AAVDJ-Syn-jGCaMP8s [49] at a titer of 1.16×10^{13} vg/ml was injected over a period of 1 min. The process was repeated for both hemispheres. The pups were then placed on a recovery box on top of a heating mat to promote recovery. The entire procedure took no more than 10 minutes per pup.

Histology

Mice were perfused transcardially with saline containing 1 mM Ca^{2+} and subsequently with 4% formaldehyde in 0.1 M phosphate buffer under deep anesthesia with isoflurane (3-4%). The brains were removed and then post-fixed with the same fixative for at least 12 h at 4°C. The brains were then cut into coronal sections with a thickness of 50 μm using a microslicer (VT1000S, Leica, Wetzlar, Germany). The serial sections were cover-slipped with mounting medium (DAPI Fluoromount-G, Southern Biotech, AL, USA). GCaMP and DAPI were visualized through a fluorescence microscope (IX83 inverted microscope, Olympus, Tokyo, Japan).

Head plate surgery

Mice were anesthetized with isoflurane (1-1.5%) and the body temperature was monitored with a rectal thermometer. Eye ointment was applied to keep the eyes moist. Head plate surgery was conducted on mice over 8 weeks of age. A custom head-fixing imaging chamber [50] was mounted on the skull with a self-cure dental adhesive resin cement (Super bond, L-Type Radiopaque; Sun Medical) and luting cement (FUJI LUTE BC; GC Dental). The ample width of the head plate allowed the implantation of a 7 mm × 7 mm glass plug and subsequent large field-of-view two-photon imaging. The surface of the intact skull was then coated with

clear acrylic dental resin (Super bond, Polymer clear; Sun Medical) and silicone to prevent drying.

Cranial window implant

More than three days after head plate surgery, an ultra-large cranial window implant [23,51] was performed as follows. The glass plug used to cover dorsal cortex was made with a 6 mm × 6 mm #3 cover slip and a 7 mm × 7 mm #0 coverslip which were custom-made by Matsunami Glass Ind. Two coverslips were glued together using optical adhesive (Norland Optical Adhesive 63; Norland Products). After anesthesia, 4 µl/g body weight of 20 % mannitol solution was administered via intraperitoneal injection to reduce brain swelling, and 0.216 µg/g of atropine sulfate was administered intraperitoneally to reduce saliva and mucus secretion. The mouse head plate was fixed after anesthesia. Clear acrylic dental resin was removed using a dental drill, followed by marking of bregma and stereotaxic coordinates. The skull along the outline of the cranial window as well as coronal and sagittal sutures was thinned with the drill. The frontal and parietal bones were removed in four separate pieces. The glass plug was then placed on the exposed cortex, enabling optical access to the entire dorsal cortex. The glass plug was attached to the bone with cyanoacrylate glue and secured using dental resin cement. After the surgery, meloxicam was injected subcutaneously and 12 µl/g body weight of 20 % mannitol solution was administered via intraperitoneal injection.

Two-photon imaging

Two-photon imaging was conducted with a custom-made mesoscope, Diesel2p [29]. For excitation of GCaMP, we used a fixed-wavelength fiber laser, ALCOR 920-2 (920 nm, 80 MHz) (Spark laser, France). Group-delay dispersion (~60,000 fs²) was pre-compensated inside the laser head by maximizing sample fluorescence. Laser power was regulated with a half-wave plate followed by a polarizing beam-splitter cube. The beam was then expanded two- or three-fold (×3 beam expander, Thorlabs) to fill the objective's back aperture. Beam steering employed a resonant scanner (CRS 8 kHz, Cambridge Technology) in series with two galvanometric mirrors (R6210H, Cambridge Technology), all driven by an analog output board (PCI-6722, National Instruments). Custom scan and tube lenses, a primary dichroic mirror, the objective, and the collection optics completed the optical path. The sample power was usually 80-100 mW and never exceeded 135 mW in any experiment. The imaging depth was at layer 2/3 (100-150 µm from pia). Fluorescence was routed through the dichroic mirror and a 700 nm short-pass emission filter (FESH0700, Thorlabs) and detected by a GaAsP photomultiplier tube (H10770PA-40, Hamamatsu). The signal was amplified (#59-179, Edmund Optics) and digitized at 12 bit, 10 MS/s (ATS-460, AlazarTech). A line-sync signal from the resonant scanner provided the master clock for all devices. Custom LabVIEW software (LabVIEW 2019, National Instruments) controlled acquisition. Imaging was performed in two FOVs, each with size 4.25 × 1.5 mm^2, yielding a total FOV of 4.25 × 3 mm^2. Images were acquired at 2,000 × 1,168 pixels and sampled at 3.59 frames per second.

One-photon calcium imaging

One-photon calcium imaging was conducted more than two days before or more than three days after two-photon calcium imaging on the platform. Mice were imaged under head-fixed conditions. Excitation light for GCaMP was delivered in a dark enclosure. A 470 nm blue LED (M470F4, Thorlabs) was positioned 15° above the right hemisphere. Emitted light passed an 85 mm F/2 lens, a 50 mm F/1.4 lens, and a 525/39 nm filter before reaching a CMOS camera (504 × 504 pixels, 14.1 µm pixel size after 3 × 3 binning) (Alvium USB 3.1, Allied Vision).

Frames were acquired at 20 frames per second under LabVIEW control (National Instruments). Recordings were conducted in an awake state and lasted less than 30 min.

Sensory stimulation

For sensory stimulation of mice, a plastic pipette was attached to the membrane of a speaker. The pipette was then attached to either the tail, trunk or right/left whisker of the head-fixed mouse. In each 8-s trial, there was a 50 Hz stimulation for 0.8 s, and each body part was stimulated for 60 trials. The activity of the dorsal cortex was recorded through one-photon calcium imaging. The location of peak response to each stimulation was mapped and aligned with mouse brain atlas [52] to identify the corresponding cortical areas.

Image processing

Image preprocessing was done using ImageJ (National Institutes of Health) and MATLAB (MathWorks, Natick, MA, USA) software. The bidirectional phase offset of the image was calculated, and sinusoidal distortions caused by the resonant scanner were corrected. TurboReg plugin [53] on ImageJ was used for image registration. By utilizing ImageJ macros, the images were divided into 9 by 8 smaller blocks, and registration was performed for each block. Subsequently, MATLAB was used to combine the drift-corrected images from each block. The X- and Y-offsets for each block were obtained by linearly interpolating the mean offset values across all pixels, thereby ensuring spatially consistent shifts. The registered images were then analyzed using Suite2p [54] to determine the location of the regions of interest (ROIs). The intensity of each ROI was calculated by subtracting mean values of background pixels within 120 μm of the ROI excluding the other ROIs from the mean value of the ROI. For each ROI, the 8th percentile pixel value within a 15-s time window was obtained, which was then smoothed using a Gaussian filter with standard deviation of 30 s. This was considered as the baseline of neural activity, and was subtracted from the original data to set the baseline to 0. A Wiener filter with temporal length of 1.7 s was applied to reduce noise. Non-negative deconvolution with a time constant of 0.48 s for GCaMP8s and 1.2 s for mouse GCaMP6s (fast-oopsi; [55]) was performed, and a Gaussian filter with standard deviation of 0.2 s was applied at the end. We defined the time-series data for each ROI as its "activity." ROIs whose activity skewness exceeded 0.5 were classified as active neurons (or simply "neurons"), and only these were included in analyses. For analysis, the neural data were interpolated to have a 10 Hz signal rate.

Platform motion during two-photon imaging

We delivered five types of platform motion to each animal during two-photon calcium imaging (**Fig. 2b**).

1. **8DT (8-direction tilt):** Each trial consisted of a 10° tilt over 1.5 s toward one of eight possible directions, followed by a 1.5-s return to baseline. Trials were separated by a 1-s inter-trial interval. To prevent the mouse from predicting the upcoming tilt direction, the sequence was constructed so that every possible pair of consecutive directions occurred exactly once while maintaining equal presentation of all directions. This required 65 trials in total from which the first trial was omitted for analysis, resulting in 64 trials (8 per direction). The tilt trajectory was generated using a cosine profile to provide smooth acceleration and deceleration.
2. **T-Rot (Tilted-rotation):** The platform was tilted 10° forward and, while maintaining this tilt, rotated clockwise for 10 full revolutions (4 s per revolution). Each block therefore comprised 10 trials, but the first trial was omitted from analysis, leaving 9 trials in total.

3. **Roll (left–right tilt):** The platform was initially tilted 10° to the left and then seesawed back and forth between left and right. Each cycle lasted 4 s and was repeated 10 times. To ensure smooth acceleration and deceleration, the tilt angle followed a cosine profile. As with the other motion types, the first trial was omitted from analysis, leaving 9 trials in total.
4. **Yaw (horizontal rotation):** The platform rotated about its central vertical axis by ±15° and oscillated back and forth. Each cycle lasted 4 s and was repeated 10 times. The rotation followed a cosine profile to ensure smooth acceleration and deceleration. As with the other motion types, the first trial was omitted from analysis, leaving 9 trials in total.
5. **Vert (vertical translation):** The platform translated vertically between +5 mm and −5 mm in an oscillatory motion. Each cycle lasted 4 s and was repeated 10 times. The translation followed a cosine profile to ensure smooth acceleration and deceleration. As with the other motion types, the first trial was omitted from analysis, leaving 9 trials in total.

Each session was composed of repeated motion blocks, with each block consisting of T-Rot (10 trials), Roll (10 trials), Yaw (10 trials), Vert (10 trials), and 8DT (65 trials). Each block was repeated 6–8 times within a session, resulting in a total session duration of 42–56 minutes. Neural activity was stably recorded during these platform motions, allowing us to sample the same neuronal population across conditions. Details of the newly developed platform (capable of generating arbitrary ground motions including those above), its operating principles, components and hardware, software, motion parameters, and comparisons with existing systems are provided in the **Supplementary Information**.

Platform motion performance assessment

To evaluate the accuracy of platform motion, we conducted repeated translational movements along the x-axis. The platform was programmed to follow a cosine trajectory with an amplitude of ± 50 mm relative to its default position. Each trial lasted 1,200 ms, and the motion was repeated 10 times. A 5 × 6 checkerboard pattern was affixed to the platform surface to enable motion tracking. Two machine vision cameras were positioned around the platform to capture its movement at approximately 300 Hz. The recorded checkerboard positions were reconstructed into three-dimensional coordinates (see **Supplementary Information** for details). The reconstructed trajectory was then projected onto the x-axis and compared with the corresponding simulated trajectory. Velocity was estimated as the slope of a local linear fit within a 100 ms sliding window, and the resulting velocity profile was compared with the ideal velocity trajectory. In both analyses, only time points at which the checkerboard was successfully detected and the triangulation error was below 1 mm were included.

Habituation

In order to habituate animals to ground motion under head-fixed conditions, we placed head-fixed mice on a balance board with a diameter of 250 mm (HCF-BDBUL, Elecom) and randomly tilted the board for 30 minutes. The board was perturbed by a rotating zip tie attached to a stepper motor, causing random tilts, and the head-fixed mice had to maintain their balance at the center of the board. Four mice went through this habituation stage for 4 days, followed by a phase of habituation to movement on a 6DOF platform under a microscope, after which the imaging experiment was performed. Six mice were habituated directly on the 6AGM after head plate fixation habituation.

Reconstruction of 3D posture

Following the removal of hair from the mouse’s limbs and back, infrared absorptive markers were applied to their elbows, knees and three equally spaced points on the back. Four

cameras (acA720-290gm, Basler) were used to record mouse movements. The cameras were positioned at the left and right anterodorsal oblique angles and at the left and right posterodorsal oblique angles so that the animal's body remained visible even at the maximum tilt angle. Five infrared light sources (PA303 Security Light) were arranged to minimize shadows. To suppress infrared reflections, the platform was covered with an IR Flock Sheet (Musou Black, Koyo Orient Japan Co., Ltd.). The cameras were operated at 290 frames per second, and the exposure time of each camera was adjusted to 1 ms. All cameras were connected via gigabit ethernet cables to a PoE board (LAN-GIGAPOE51, Sanwa Supply). Images were acquired at 270 × 360 pixels per camera, yielding a combined field of 540 × 720 pixels across the four cameras, and were controlled and recorded using custom LabVIEW (IMAQ)-based software. DeepLabCut [56,57] was used to track left and right paws, left and right elbows, left and right toes, left and right heels, left and right knees, a point of the tail, and the three points on the back (15 points in total; **Fig. 1h**). The nose position was assumed to be a single fixed point because it does not move during head fixation. The detected points were reconstructed to 3D coordinates by triangulation. Any frames with triangulation error >4 mm were replaced by interpolated values derived from neighboring frames with error <4 mm. Velocities and accelerations were then computed from the 3D trajectories after applying a 10 Hz low-pass filter to reduce the noise from frame-to-frame inaccuracies in DeepLabCut.

For a precise triangulation, radial lens distortion correction, intrinsic parameter estimation, and stereo calibration were all performed using checkerboards (see **Supplementary Information** for details). Following radial lens distortion estimation using a two-parameter division model, 5 parameters of the pinhole camera model were linearly estimated using undistorted images. The RANSAC algorithm [58] was employed to filter out inaccurately detected checkerboards, after which the calibration parameters were refined by nonlinear optimization. Stereo calibration was performed using a normalized 8-point algorithm, similarly employing the RANSAC algorithm to filter out faulty checkerboards. The entire algorithm, with the exception of the checkerboard detection, was developed and customized in MATLAB.

We defined the angle formed by the estimated positions of the relevant body parts as the "joint" angle (**Fig. 1h**). Since an angle can be determined once three points are determined, ${}_{15}C_3 = 455$ angles can be selected from the 14 estimated body part points. We used 16 of these angles as joints (**Fig. 1h**), and the results did not change when all 455 angles were used to estimate neural activity.

Direction selectivity

Tilt direction selectivity of individual neurons was obtained from the data during 8DT motions as follows. For each neuron, baseline activity was defined as the mean activity during the horizontal condition without ground motion. For each direction, mean activity during 1–2 s after stimulus onset was measured, and the baseline activity was subtracted. Negative values were set to zero, and the resulting responses were averaged across trials for each direction. The resulting average response across directions was normalized such that their sum across all directions equaled 1. The direction selectivity score was defined as the magnitude of the vector sum of these mean responses, with each response treated as a vector whose angle corresponded to the tilt direction and whose magnitude corresponded to the mean response amplitude. The preferred direction of each neuron was defined as the direction that yielded the maximum response. Neurons with a direction selectivity score >0.1 and a significant effect of direction, assessed by one-way ANOVA across tilt directions for each neuron ($p < 0.05$), were classified as direction-selective neurons.

Encoding model

The encoding model was implemented as a ridge linear regression that explained the activity of individual neurons using environmental, postural, and movement variables. Both neuronal activity and all model variables were resampled to 10 Hz before model fitting. These variable sets—82 environmental variables, 348 postural variables, and 1,056 movement variables (1,486 variables in total)—were defined as follows.

Environmental information comprised tilt direction and tilt angle. Tilt direction was discretized into 8 spatial bins. Tilt angle was discretized into 5 bins and further separated according to the sign of tilt velocity (increasing vs decreasing tilt angle). This resulted in 10 angle bins per spatial direction and a total of 80 environmental variables. The bins were one-hot encoded and were temporally filtered with a Gaussian kernel (σ = 0.1 s). In addition to the one-hot vectors, the non-discretized tilt direction and tilt angle were included, yielding a total of 82 environmental variables.

Postural information consisted of the 3D coordinates of 14 body parts and the joint angles computed from these positions. The 3D coordinates were discretized into 5 bins individually and represented as one-hot vectors, yielding 14 (body parts) × 3 (XYZ) × 5 (bins) = 210 variables. Each joint angle was discretized into 5 bins and one-hot encoded, giving 16 × 5 = 80 variables. All one-hot–encoded time series were temporally filtered with a Gaussian kernel (σ = 0.1 s). Non-discretized variables were also included, resulting in a total of 348 postural variables, 252 variables for the 3D coordinates and 96 for the joint angles.

Movement information included, for each of the 14 body parts, velocity and acceleration along the XYZ axes, as well as their magnitudes (speed and acceleration magnitude). Each variable was discretized into 5 bins and represented as one-hot vectors. Velocities across body parts comprised 14 (body parts) × 3 (XYZ) × 5 (bins) + original (14 × 3) = 252 variables, whereas velocity magnitudes, which are scalars over XYZ, comprised 14 (body parts) × 5 (bins) + original (14) = 84 variables, including non-discretized values. Similarly, accelerations and its magnitude comprised 252 and 84 variables, respectively. The joint angular velocity, acceleration, speed, and acceleration magnitude were also discretized into 5 bins and one-hot encoded, yielding 16 (joint angles) × 5 (bins) + original (16) = 96 variables each. As above, all one-hot–encoded time series were temporally filtered with a Gaussian kernel (σ = 0.1 s). A total of 1,056 movement variables were obtained.

To assess whether platform-related information could be linearly reconstructed from posture and movement variables, we computed the variance inflation factor (VIF) for the tilt-direction parameter. Specifically, the non-discretized tilt direction variable, θ, was treated as a scalar target variable $y \in \mathbb{R}^T$, and all posture- and movement-related predictors used in the encoding model were used as the predictor matrix $\mathbf{Z} \in \mathbb{R}^{T \times r}$. After restricting the data to valid time points when the platform was tilting and centering the variables, we linearly fitted tilt direction from the posture and movement predictors and computed the coefficient of determination, R_θ^2, for this auxiliary regression. We then converted this value into a VIF as

$$\mathrm{VIF}_\theta = \frac{1}{1 - R_\theta^2}.$$

Values were summarized directly across imaging sessions, and the mean ± S.D. across sessions was reported. Additionally, we performed a body-part-specific blockwise VIF analysis. The posture/movement predictors used in the encoding model were subdivided into four anatomically defined chunks (upper limb, lower limb, trunk, and tail) using the same grouping as in the predictor-ablation analyses. For each chunk B, the corresponding encoded predictor block was treated as a multivariate target matrix $\boldsymbol{Y}_B \in \mathbb{R}^{T \times q_B}$, and all remaining predictors in

the full design matrix were used as the reference predictor matrix $\boldsymbol{Z}_{\setminus B}$. After centering the variables, we linearly fitted $\boldsymbol{Y}_B$ from $\boldsymbol{Z}_{\setminus B}$ and computed a block coefficient of determination,

$$R_B^2 = 1 - \frac{\| \boldsymbol{Y}_B - \widehat{\boldsymbol{Y}}_B \|_F^2}{\| \boldsymbol{Y}_B \|_F^2},$$

where $\|\cdot\|_F$ denotes the Frobenius norm. This value was then converted into a VIF,

$$VIF_B = \frac{1}{1 - R_B^2}.$$

Values were summarized directly across imaging sessions, and the mean ± S.D. across sessions was reported. All the VIFs were modest. These analyses indicated no evidence of severe multicollinearity between tilt-related predictors and posture/movement predictors, supporting the interpretability of the ablation-based contribution estimates.

For the full encoding model, the activity of each neuron was predicted from the complete set of explanatory variables using ridge regression. At each time point, neural activity was predicted only from the explanatory variables at the same time point; no past values or time-lagged predictors were included. Prediction accuracy was quantified by the coefficient of determination (R^2) using 10-fold cross-validation:

$$R^2 = 1 - \frac{\sum_i \left(y_i^{\text{test}} - \hat{y}_i^{\text{test}}\right)^2}{\sum_i \left(y_i^{\text{test}} - \bar{y}^{\text{train}}\right)^2},$$

where y_i^{test} is the observed activity at sample i in the test fold, $\hat{y}_i^{\text{test}}$ is the corresponding model prediction, and $\bar{y}^{\text{train}}$ is the mean activity in the training fold. Thus, R^2 quantifies prediction accuracy relative to a baseline model that predicts the training-fold mean.

The ridge regularization parameter (λ) was searched over the range from 10^2 to 10^8 in 0.5-log-unit steps, and, for each neuron, the value yielding the highest prediction accuracy was selected.

For the ablation model, a target variable group was removed and the activity of each neuron was predicted from the remaining variables using the same ridge-regression procedure. Prediction accuracy was again evaluated by 10-fold cross-validation, and λ was selected in the same way as for the full model. To quantify the contribution of the ablated variable group for each neuron, we compared the prediction accuracy of the full and ablation models using

$$\Delta R_n^2 = \frac{R_{\text{full},n}^2 - R_{\text{ablated},n}^2}{R_{\text{full},n}^2},$$

where $R_{\text{full},n}^2$ and $R_{\text{ablated},n}^2$ denote the prediction accuracy of the full and ablation models for neuron n, respectively. The null model predicted a constant value equal to the mean activity in the training fold. Thus, ΔR_n^2 represents the fraction of explainable predictive performance lost when the target variable group was removed. To visualize the cortical distribution of predictor contribution, we computed a local contribution map for each predictor group. For each pixel p, we identified neurons located within a radius of 150 μm in the cortical surface plane. Because normalized ablation scores can become unstable for neurons with low full-model prediction accuracy, only neurons with $R_{\text{full},n}^2$ above the 75th percentile were included. The map value at pixel p was then computed as the unweighted mean of ΔR_n^2 across those neurons:

$$S(p) = \frac{\sum_{n \in D(p),\, R_{\text{full},n}^2 > q_{R^2}} \Delta R_n^2}{\sum_{n \in D(p),\, R_{\text{full},n}^2 > q_{R^2}} 1},$$

where $D(p)$ denotes the set of neurons within 150 μm of pixel p, and q_{R^2} is the 75th percentile of R^2_{full} across neurons.

We also computed a local proportion map to visualize the spatial enrichment of neurons with strong predictor contribution among neurons that were well predicted by the full model. For each pixel p, we calculated the fraction of nearby neurons satisfying $R^2_{\text{full},n} > q_{R^2}$ whose ΔR^2_n exceeded $q_{\Delta R^2}$, where $q_{\Delta R^2}$ is the 75th percentile of ΔR^2 across neurons satisfying $R^2_{\text{full},n} > q_{R^2}$:

$$P_{\text{rel}}(p) = \frac{\sum_{n \in D(p),\, R^2_{\text{full},n} > q_{R^2},\, \Delta R^2_n > q_{\Delta R^2}} 1}{\sum_{n \in D(p),\, R^2_{\text{full},n} > q_{R^2}} 1}.$$

Thus, $P_{\text{rel}}(p)$ represents the local fraction of well-predicted neurons that showed a strong loss of performance after ablation.

In addition, we computed an absolute local proportion map:

$$P_{\text{abs}}(p) = \frac{\sum_{n \in D(p),\, R^2_{\text{full},n} > q_{R^2},\, \Delta R^2_n > q_{\Delta R^2}} 1}{\sum_{n \in D(p)} 1}.$$

Thus, $P_{\text{abs}}(p)$ represents the local fraction of all neurons that showed both high full-model prediction accuracy and a strong loss of performance after ablation.

Visualization was restricted to pixels with more than 50 neurons within the 150 μm radius, and pixels not meeting this criterion were excluded. No additional distance weighting was applied within the local neighborhood.

For each neuron, estimating a statistical p-value for the full model would require approximately 1,000 shuffle controls, followed each time by refitting the ridge-regression model. Estimating p-values for each parameter would require the same number of shuffles. Applying this procedure to approximately 130,000 neurons was computationally infeasible. By contrast, the goal of this analysis was not to determine the exact statistical significance of each neuron, but to extract a subset of neurons whose scores exceeded chance level for each parameter and to use these subsets to generate the maps. We therefore evaluated, as described below, which percentile threshold among the top 20%, 25%, and 30% best corresponded to a statistically significant subset of neurons. Based on this analysis, we fixed the threshold at the top 25%. The 75th percentile of full-model R^2 corresponded to an empirical block-permutation p-value of 0.0015. For predictor-contribution thresholds, the empirical p-values varied across predictor groups and are reported in **Extended Data Fig. 5c**. We also confirmed that the qualitative spatial distributions of the maps were not substantially changed when the top 20%, 25%, or 30% thresholds were used.

We performed empirical block-permutation null analyses. These analyses were designed to test the population-level thresholds used for visualization. For the full-model threshold analysis, we used a neural block-permutation null. From each session, 1,000 active neurons were randomly sampled. For each sampled neuron, the neural activity trace was divided into contiguous 5-s blocks, and the order of these blocks was randomly permuted while keeping the predictors unchanged. The full ridge-regression encoding model was then refit to the block-permuted neural activity using the same cross-validation and regularization procedure as in the original encoding analysis.

The empirical p-value, $p_{\text{full,null}}$, for the null full-model was calculated as the proportion of null full-model scores $R^2_{\text{full,null}}$ that exceeded the observed full-model threshold, q_{R^2}:

$$p_{\text{full,null}} = \frac{1 + \sum I\left(R^2_{\text{full,null}} \geq q_{R^2}\right)}{1 + N_{\text{null}}}.$$

Here, N_{null} denotes the total number of sampled null neurons pooled across recording sessions.

For the predictor-contribution thresholds, we performed a separate predictor-family block-permutation analysis. To construct the null distribution for each predictor family, the target predictor family was divided into contiguous 5 s blocks, and the block order was permuted in time. For each predictor family g, we refit the full model after block-permuting only that predictor family, obtaining $R^2_{g,\text{null}}$. The null contribution statistic was then computed using the observed ablation-model and observed full-model scores as references:

$$\Delta R^2_{g,\text{null}} = \frac{R^2_{g,\text{null}} - R^2_{\text{ablated}}}{R^2_{\text{full}}}.$$

where R^2_{ablated} is the prediction accuracy of observed ablation-model and R^2_{full} is the observed full-model accuracy.

This null statistic was evaluated only for sampled neurons whose full model prediction accuracy exceeded the observed full-model threshold q_{R^2}. The empirical p-value for each predictor-family contribution threshold was calculated as

$$p_{g,\text{null}} = \frac{1 + \sum I\left(\Delta R^2_{g,\text{null}} \geq q_{\Delta R^2_g}\right)}{1 + N_g},$$

where N_g is the number of sampled neurons included in the conditional null distribution for predictor family g and $q_{\Delta R^2_g}$ is the observed contribution threshold for predictor family g.

Because refitting the full and ablated encoding models for many repeated random permutations of every neuron and predictor family would be computationally expensive, we did not perform multiple independent permutations for each individual neuron. Instead, we constructed a population-level empirical null distribution by applying one independently generated block permutation to each sampled neuron and pooling the resulting null scores across neurons and recording planes. Thus, the resulting p-values quantify how extreme the observed population-level 75th-percentile thresholds were under the corresponding block-permutation null model.

Statistical test for the spatial localization

Spatial similarity among the maps associated with somatotopy (forelimb, hindlimb, trunk, and tail), ground-tilt, and eigenpostures 1–4 was statistically analyzed using a spatial block permutation test as follows. The goal of this analysis was to compare the similarity to the tilt map between any pair of the other maps. First, we computed pixel-wise Pearson correlation coefficients between the tilt map and each of the other maps, denoted as

$$r_{tilt,i}\ (i = 1,2,\ldots,8),$$

where i corresponds to forelimb, hindlimb, trunk, tail, and eigenpostures 1–4, respectively.

For each pair of non-tilt maps i and j, we defined the difference in similarity to the tilt map as

$$r_{tilt,i,j} = r_{tilt,i} - r_{tilt,j}.$$

To construct a null distribution while preserving spatial autocorrelation, we divided the maps into square blocks of 250 μm × 250 μm, arranged in a 10 × 16 grid over a field of view centered on S1tr. In each iteration, the blocks were randomly shuffled, and $r_{tilt,i,j}$ was recalculated for the shuffled data, yielding $r^{shuffle}_{tilt,i,j}$. This shuffling procedure was repeated 10,000 times to obtain the null distribution. A one-sided *p* value was computed as the rank of the observed

$r_{tilt,i,j}$ within the null distribution, $r_{tilt,i,j}^{shuffle}$, testing whether the similarity between the tilt map and map i was significantly greater than that between the tilt map and map j.

Decoding analysis

We decoded tilt-related variables (8DT, T-Rot, Roll), vertical position (Vert), and horizontal rotation angle (Yaw). All decoding analyses used bagged decision trees (MATLAB function *TreeBagger*). The number of trees was fixed at 100. For 8DT and T-Rot, tilt directions were discretized into eight categories spaced 45° apart, and decoding was performed as a classification problem. For Roll, Vert, and Yaw, decoding was performed as a regression problem. To prevent overfitting, we performed 10-fold cross-validation, and decoding performance was quantified by classification accuracy for classification tasks and by the coefficient of determination (R^2) for regression tasks. When comparing decoding performance across regions, we randomly sampled 200 neurons from the target region, reduced the data to 20 dimensions by PCA, and then performed decoding. For each session, regions with fewer than 200 neurons were omitted from analysis. The decoding was repeated 10 times for each session. When decoding with all areas combined, as well as for the frontal cortex and parietal cortex analyzed separately, the data were reduced first to 1,000 dimensions by PCA and then to 100 dimensions by cPCA ($w = 0.5$), and decoding was performed on the resulting 100-dimensional representation. In GCARP, decoding was performed on the 100-dimensional GCCA representation or on the corresponding 99-dimensional representation obtained after excluding one component. Because dimensionality reduction must be integrated with cross-validation, the dimensionality-reduction model was fitted on each training fold and the resulting transform was applied to the corresponding test fold.

Mutual information was calculated from the confusion matrix between the true and decoded labels. For each true label, the confusion matrix was normalized to represent the conditional probability of each decoded label, and the resulting matrix was used to quantify the reduction in uncertainty about the true label provided by the decoded label. Mutual information was calculated as the mutual dependence between true and decoded labels and was reported in bits.

GCCA (Generalized Canonical Correlation Analysis)

To extract latent components shared across eight cortical areas, we employed generalized canonical correlation analysis (GCCA) [23,30]. GCCA extends conventional canonical correlation analysis (CCA), which identifies maximally correlated linear projections of two datasets, to more than two datasets, thereby enabling estimation of a common low-dimensional representation shared across multiple brain regions. For each region, neural activity was first reduced to 100 principal components using principal component analysis (PCA), and the resulting component time series were z-scored across time before GCCA.

Let $X_i \in \mathbb{R}^{T \times d_i}$ denote the PCA-reduced data matrix for region i, where T is the number of time points and d_i is the number of retained dimensions. We sought a shared latent time course $y \in \mathbb{R}^T$ that can be approximated from each region by a linear combination of its activity. We used a distance-to-subspaces formulation of GCCA:

$$\min_{y,\{w_i\}} \sum_{i=1}^{v} \| y - X_i w_i \|_2^2 \quad s.t. \quad \| y \|_2 = 1.$$

For fixed y, the optimal weights are given by least squares:

$$w_i = X_i^{\dagger} y,$$

where † denotes the Moore–Penrose pseudoinverse. Substituting this expression back into the objective yields:

$$\min_{\|y\|_2=1} \; y^\top \left(\sum_{i=1}^{v} (I - P_i) \right) y,$$

where

$$P_i = X_i X_i^\dagger$$

is the orthogonal projector onto the column space of X_i. Thus, the shared trajectory y is obtained as the eigenvector corresponding to the smallest eigenvalue of

$$A = \sum_{i=1}^{v} (I - P_i).$$

To obtain an m-dimensional shared subspace $Y \in \mathbb{R}^{T \times m}$, we took the eigenvectors associated with the m smallest eigenvalues of A. The corresponding region-specific weights are

$$W_i = X_i^\dagger Y.$$

This formulation identifies latent time courses that are simultaneously close to the column spaces of all recordings, yielding a consensus representation shared across cortical areas. For cross validation, the training fold was used to obtain W_i and the shared trajectory Y for the test fold was obtained using the above distance-to-subspaces optimization function, yielding

$$\hat{Y}_{\text{test}} = \frac{1}{v} \sum_{i=1}^{v} X_i^{\text{test}} W_i.$$

GCARP (Generalized Canonical component-ablation-based representational probing)

GCARP is an extension of CARP for two-area datasets to multi-area datasets [23]. Two hundred neurons were randomly sampled from each area, which were then reduced to 100 dimensions using PCA. The dimensionally reduced time series from all areas were then transformed into a 100-dimensional representation using GCCA. Using this representation, decoding of movement, ground-tilt, and eigenposture was performed in the same manner as described above. Movement was defined as the mean speed of all the body parts. Ground-tilt was decoded through classification after dividing it into 8 bins, 45° apart. The decoding accuracy obtained here was regarded as the maximal decoding performance. Next, the *N*-th GCCA dimension (*N*=1,2,…,10) was removed, and decoding was repeated with the remaining dimensions. The reduction in decoding accuracy relative to the maximal performance was interpreted as the contribution of the *N*-th component.

cPCA and gcPCA

To extract the informative dimensions from the neural data, we used cPCA [23,59] or generalized cPCA (gcPCA). For analyses using the full population, neural activity was first projected onto the first 1000 principal components using standard PCA. For brain-region-wise analyses, the same preprocessing was applied only when a region contained more than 1000 neurons whereas regions with 1000 or fewer neurons were analyzed directly without this initial PCA step. This initial PCA step was used to reduce sensitivity to sampling noise and stabilize the subsequent eigen decomposition while preserving the dominant population-level activity. The resulting neural data used for cPCA and gcPCA was arranged as an array $X \in \mathbb{R}^{R \times T \times N}$, where R is the number of trials, T the number of time points, and N the number of neural

dimensions. For each dataset, we computed two covariance matrices in neuron space: a within-trial (temporal) covariance, obtained by centering each trial across time and accumulating cross-products, and an across-trial covariance, obtained by centering across trials at each time point and accumulating cross-products. Each covariance was normalized by its trace to remove trivial scaling effects. cPCA then forms a weighted combination

$$\Sigma(w) = (1-w)\,\Sigma_{\text{within}} - w\,\Sigma_{\text{across}}, \qquad w \in [0,1],$$

and identifies axes $\mathbf{v}$ that maximize $\mathbf{v}^{\top}\Sigma(w)\mathbf{v}$ subject to $\|\mathbf{v}\|_2 = 1$. The resulting cPCA components are given by the leading eigenvectors of $\Sigma(w)$. Unless otherwise noted, we set $w = 0.5$ When $w = 0$, the method reduces to standard PCA. As w increases, the contribution of within-trial covariance decreases, while the penalty on across-trial covariance increases. As a result, the selected axes increasingly prioritize minimizing across-trial variance rather than maximizing within-trial variance.

For gcPCA, we further incorporated an additional covariance term to suppress activity associated with a second motion type. Specifically, we constructed a weighted covariance matrix of the form

$$\Sigma(w_1, w_2) = (1-w_1)\,\Sigma^{(1)}_{\text{within}} - w_1\,\Sigma^{(1)}_{\text{across}} - w_2\,\Sigma^{(2)}_{\text{within}},$$

where superscripts (1) and (2) denote motion type 1 (the target condition) and motion type 2 (the condition to suppress), respectively. gcPCA axes were obtained as the leading eigenvectors of $\Sigma(w_1, w_2)$, and projections were computed by multiplying population activity vectors by these eigenvectors. When $w_1 = w_2 = 0$ the method reduces to standard PCA, and when $w_2 = 0$, it reduces to cPCA. As w_2 increases, variance associated with motion type 2 is increasingly penalized, causing the selected axes to preferentially suppress neural dimensions that strongly covary with motion type 2. We varied w_2 in the range from 0 to 3.

In the 8DT, we concatenated the 3-s responses for the eight directions to form a 24-s trajectory per trial; with ~50 repetitions sampled at 10 Hz, this corresponds to $T \approx 240$ time points and $R \approx 50$ trials per neuron.

Because cPCA is a special case of gcPCA, we describe the derivation only for gcPCA. For K components, gcPCA was formulated as the following constrained maximization problem

$$\max_{V_K} \operatorname{tr}\left(V_K^{\top}\Sigma(w_1, w_2)V_K\right)$$

subject to

$$V_K^{\top}V_K = I_K,$$

where $V_K = [v_1, \ldots, v_K]$ contains K orthonormal projection axes. Using a Lagrange multiplier, this optimization reduces to the eigenvalue problem

$$\Sigma(w_1, w_2)v = \lambda v.$$

Thus, gcPCA components were obtained as the eigenvectors of $\Sigma(w_1, w_2)$, ordered by decreasing eigenvalue. The neural activity vector x_{rt} was then projected onto the low-dimensional gcPCA space as

$$z_{rt} = V_K^{\top}x_{rt},$$

where $V_K = [v_1, \ldots, v_K]$ contains the first K eigenvectors as columns.

For visualization, neural trajectories in the first three cPCA or gcPCA dimensions were averaged across non-overlapping groups of up to five trials, and each group average was plotted separately.

Ellipse fitting

To quantify the geometric structure of population trajectories in two-dimensional gcPCA space, we fit ellipses to the projected point clouds. An ellipse was parametrized by its center $(x_0,\ y_0)$, semi-major and semi-minor axes $(a,\ b)$, and rotation angle ϕ. In rotated coordinates,

$$\left(\frac{x'}{a}\right)^2 + \left(\frac{y'}{b}\right)^2 = 1,$$

where x', y'denote coordinates after translation and rotation by (x_0, y_0, ϕ).

Fitting was performed in two stages. First, an initial estimate was obtained using a direct least-squares conic fit. Second, parameters were refined by minimizing the sum of orthogonal Euclidean distances from data points to the ellipse,

$$\min_{\theta} \sum_{i=1}^{n} \rho\left(d_i(\theta)\right),$$

where $d_i(\theta)$ denotes the shortest distance from point i to the ellipse and $\rho(\cdot)$ is a soft-L1 robust loss. Optimization was performed using a trust-region reflective algorithm (SciPy).

To prevent unstable solutions when data covered only partial arcs, parameter bounds were imposed and weak regularization on axis lengths was applied. After optimization, we enforced $a \geq b$. Ellipse area was computed as πab, and axis ratio was defined as a/b.

Persistent homology (PH) analysis

To evaluate the topological structure of the tilt-space in higher-dimensional representations, we performed persistent homology analysis. First, neural population activity data for each condition (T-Rot, 8DT, and Vert) were reduced to five dimensions using gcPCA. We chose five dimensions to characterize structure beyond two-dimensional visualization while retaining a compact representation. Next, 5-trial averaged neural activity vectors at each time point were treated as point cloud data, and Vietoris–Rips complexes were constructed based on pairwise Euclidean distances [36]. In PH analysis, the distance scale (filtration) was continuously increased, and spheres centered at each data point were expanded to track the emergence and disappearance of topological structures inherent in the point cloud. In this study, we focused on the first homology group (H1) and analyzed topological features corresponding to ring structures. For each H1 cycle with birth b and death d, we defined its lifetime as $d - b$. Using the resulting H1 barcodes, we compared the stability of ring structures across conditions and across each value of w_2. Maximum lifetimes were normalized within each condition by dividing by the corresponding value at $w_2 = 0$, and the resulting ratios were subjected to statistical analysis. Persistent homology was computed using Ripser [60].

Persistent landscape ringness index (LRI)

To quantify the dominance of H1 cycles, we introduced a ringness index based on the persistent landscape representation [37]. Here, t denotes the filtration parameter, corresponding to the distance scale used to connect points in the point cloud. In the persistence landscape framework, each bar (b_i, d_i) in the persistence diagram is transformed into a tent-shaped function that is zero outside the interval $[b_i, d_i]$. For each value of t, these functions were sorted in descending order, and the i-th largest value was denoted $\lambda_i(t)$. The collection of functions $\{\lambda_i(t)\}$ constitutes the persistence landscape. Using these components, we defined the ringness index as

$$\mathrm{LRI} = \frac{\int_0^{t_{\max}} \lambda_1\,(t)\,dt}{\sum_{i=1}^{k_{\max}} \int_0^{t_{\max}} \lambda_i\,(t)\,dt}.$$

where $k_{\max}$ denoted the number of landscape layers included in the normalization. In practice, we set $k_{\max} = 10$, which captured the dominant H_1 features while reducing sensitivity to a large number of small spurious cycles.

When a single dominant ring structure is present, $\lambda_1(t)$ accounts for most of the landscape mass and the LRI approaches 1. In contrast, when multiple cycles of comparable persistence coexist, the landscape mass is distributed across higher layers and the LRI decreases toward 0. Because both numerator and denominator scale identically under global rescaling of the filtration parameter, the LRI is invariant to overall metric scaling. This property enabled fair comparison across conditions in which overall variance changes with w_2, such as in the Vert condition.

Quantifying the overlap between the broadcast subspace and the tilt subspace

To quantify the relationship between the gcPCA tilt subspace and the GCCA broadcast subspace, we measured the fraction of squared norm of each GCCA axis that lay within the gcPCA subspace. To evaluate this at the level of the full cortical population, we partitioned both the gcPCA axes and the GCCA weight vectors by cortical area and concatenated the corresponding regional blocks across areas.

Let

$$G_i \in \mathbb{R}^{n_i \times d_g}$$

denote the first d_g normalized gcPCA axes restricted to neurons in region i, and let

$$w_{i,j} \in \mathbb{R}^{n_i}$$

denote the normalized GCCA weight vector for GCCA dimension j restricted to the same neurons.

We constructed a pooled gcPCA basis by vertically concatenating the regional gcPCA matrices,

$$G_{\text{all}} = \begin{bmatrix} G_1 \\ G_2 \\ \vdots \\ G_v \end{bmatrix} \in \mathbb{R}^{N \times d_g},$$

where $N = \sum_{i=1}^{v} n_i$ is the total number of neurons across all regions and v is the number of cortical areas.

Similarly, for each GCCA dimension j, we constructed a pooled GCCA weight vector

$$w_j^{\text{all}} = \begin{bmatrix} w_{1,j} \\ w_{2,j} \\ \vdots \\ w_{v,j} \end{bmatrix} \in \mathbb{R}^{N}.$$

Because restriction of gcPCA axes to regional neuron subsets can break orthogonality, the projector onto the pooled gcPCA subspace was computed as

$$P_G = G_{\text{all}} \left(G_{\text{all}}^{\top} G_{\text{all}} \right)^{\dagger} G_{\text{all}}^{\top}.$$

The overlap between each GCCA axis and the gcPCA tilt subspace was quantified as

$$f_j^2 = \frac{\left(w_j^{\text{all}} \right)^{\top} P_G w_j^{\text{all}}}{\left(w_j^{\text{all}} \right)^{\top} w_j^{\text{all}}}.$$

This measure corresponds to the fraction of the GCCA axis that lies within the pooled gcPCA subspace across the entire recorded population.

In this formulation, the gcPCA axes from all regions are treated collectively as defining a single global tilt-related subspace across the cortex. The analysis then asks how much of each GCCA axis aligns with this global gcPCA subspace. A large value indicates that the population

activity pattern captured by that GCCA axis can largely be reconstructed from the gcPCA tilt subspace when considering the full set of recorded neurons.

Computational resources

Encoding and decoding analyses, GCARP, and persistent homology computations were performed on the TSUBAME 4.0 supercomputer with HPE Cray XD665 nodes equipped with AMD EPYC 9654 CPUs and NVIDIA H100 GPUs. Depending on the requirements of each analysis, jobs were executed on either “node_q” nodes (48 AMD EPYC 9654 CPU cores, approximately 192 GB of RAM, and one NVIDIA H100 GPU) or “cpu_80” nodes (CPU-only nodes with 80 CPU cores and approximately 184 GB of RAM). Typically, 20 nodes were used in parallel, with larger node counts used for some parameter-search analyses.

Statistics

Wilcoxon’s rank-sum test, Wilcoxon’s signed-rank test, and Pearson’s or Spearman’s correlation coefficients were used for pairwise comparisons. Bonferroni correction was applied for multiple comparisons. For preferred-direction distributions, overall deviation from uniformity was tested with a χ^2 goodness-of-fit test, followed by one-sided exact binomial tests with Bonferroni correction. To compare the proportion of direction-selective neurons across cortical areas, Pearson’s χ^2 test of independence was used, followed by one-sided Fisher’s exact tests with Bonferroni correction for post hoc comparisons. Data were presented as mean ± s.e.m. unless otherwise noted.

Acknowledgements

We thank S. Kato and K. Kobayashi for AAV production, H. Mori, S. Oota, O. Ooishi and H. Kasai for discussions, all other members of the Isomura lab for supporting this work. This work was supported by JP22wm0525007 (RH), JP19dm0207089 (YI) from AMED, JP22H02731 (RH), JP20K22678 (RH), JP21B304 (RH), JP21H05134 (RH), JP21H05135 (RH), JP21H05242 (YI), and JP23H02589 (YI) from MEXT/JSPS, JPMJCR1751 (YI) from JST, Nakatani Foundation (RH), Shimadzu Foundation (RH), Takeda Science Foundation (RH), The Precise Measurement Technology Promotion Foundation (RH), Tateishi Science and Technology Foundation (RH), and Research Foundation for OptoScience and Technology (RH). This work utilized the TSUBAME4.0 supercomputer at the Institute of Science Tokyo for analysis.

Author Contributions

F.I., Ri.H. conceived the project. F.I., H.I. conducted experiments and data analysis. F.I. designed and manufactured the 6AGM. Re.H. conducted pilot experiments. Y.I. supervised the project. Ri.H., F.I. wrote the paper with the comments of all authors.

Competing Interests

The authors declare no competing interests.

Data Availability

The experimental datasets will be made publicly available on Figshare upon acceptance of the paper. At this stage, datasets containing neural activity, control parameters, and keypoint coordinates have been provided in a form accessible to the editor.

Code Availability

The software package for operating the 6AGM, including the LabVIEW, MATLAB, and Python scripts, will be released as a ZIP file on GitHub upon acceptance of the paper. At this stage, it has been provided in a form accessible to the editor.

Supplementary Information

The supplementary information includes details on 6AGM and camera calibration.

Supplementary Video

Supplementary Video 1. Configuration of the 6AGM

The components of the 6AGM and their assembly are shown in a simulated video. The configuration and design of all 6AGM components are publicly available, allowing the system to be customized. See the **Supplementary Information** for details.

Supplementary Video 2. Example demonstrating the motion capability of the 6AGM

This video was created to demonstrate the motion range and speed of the 6AGM. The system was designed with greater degrees of freedom and versatility than those required for the five motion types used in this study and can be applied to a broader range of experimental applications.

Supplementary Video 3. Three-dimensional reconstruction from four-camera images

Fifteen key points were identified from images acquired with four 290-fps cameras (left) and used for three-dimensional reconstruction (right). DeepLabCut-based tracking was facilitated by marking the shaved skin with black ink.

Supplementary Video 4. Simulated 6AGM movements corresponding to five motion types

Simulated movements of the 6AGM corresponding to the five motion types are shown. The video is played back in real time.

Supplementary Video 5. Large-field-of-view two-photon calcium imaging data

Representative two-photon calcium imaging data acquired during platform motion. The left panel shows a 4.25 mm × 3 mm field-of-view. To reduce the data size, the original sampling rate of 3.59 fps was downsampled to 1 fps, and the images were compressed and converted into a 15-fps MPEG movie. The right panels show magnified views of three 360 μm × 360 μm square regions.

Supplementary Video 6. Neural population trajectories reduced to three dimensions by gcPCA

Neural population activity trajectories reduced to three dimensions by gcPCA are shown. Color coding of responses to the five motion types follows **Fig. 4j–n**.

References

1. Takakusaki, K. Functional neuroanatomy for posture and gait control. *J. Mov. Disord.* **10**, 1–17 (2017).
2. Deliagina, T. G., Beloozerova, I. N., Zelenin, P. V. & Orlovsky, G. N. Spinal and supraspinal postural networks. *Brain Res. Rev.* **57**, 212–221 (2008).
3. MacKinnon, C. D. Sensorimotor anatomy of gait, balance, and falls. *Handb. Clin. Neurol.* **159**, 3–26 (2018).
4. Angelaki, D. E. & Laurens, J. Time course of sensory substitution for gravity sensing in visual vertical orientation perception following complete vestibular loss. *eNeuro* **7**, ENEURO.0021-20.2020 (2020).
5. Rosenberg, A. & Angelaki, D. E. Gravity influences the visual representation of object tilt in parietal cortex. *J. Neurosci.* **34**, 14170–14180 (2014).
6. Jacobs, J. V. & Horak, F. B. Cortical control of postural responses. *J. Neural Transm. (Vienna)* **114**, 1339–1348 (2007).
7. Beloozerova, I. N. *et al.* Activity of different classes of neurons of the motor cortex during postural corrections. *J. Neurosci.* **23**, 7844–7853 (2003).
8. Adkin, A. L., Quant, S., Maki, B. E. & McIlroy, W. E. Cortical responses associated with predictable and unpredictable compensatory balance reactions. *Exp. Brain Res.* **172**, 85–93 (2006).
9. Chiou, S.-Y., Hurry, M., Reed, T., Quek, J. X. & Strutton, P. H. Cortical contributions to anticipatory postural adjustments in the trunk. *J. Physiol.* **596**, 1295–1306 (2018).
10. Solis-Escalante, T. *et al.* Cortical dynamics during preparation and execution of reactive balance responses with distinct postural demands. *Neuroimage* **188**, 557–571 (2019).
11. Boebinger, S. *et al.* Precise cortical contributions to sensorimotor feedback control during reactive balance. *PLoS Comput. Biol.* **20**, e1011562 (2024).
12. Angelaki, D. E. *et al.* A gravity-based three-dimensional compass in the mouse brain. *Nat. Commun.* **11**, 1855 (2020).

13. Dougherty, J. B., Disse, G. D., Bridges, N. R. & Moxon, K. A. Effect of spinal cord injury on neural encoding of spontaneous postural perturbations in the hindlimb sensorimotor cortex. *J. Neurophysiol.* **126**, 1555–1567 (2021).
14. Disse, G. D. *et al.* Neural ensemble dynamics in trunk and hindlimb sensorimotor cortex encode for the control of postural stability. *Cell Rep.* **42**, 112347 (2023).
15. Nandakumar, B., Blumenthal, G. H., Pauzin, F. P. & Moxon, K. A. Hindlimb somatosensory information influences trunk sensory and motor cortices to support trunk stabilization. *Cereb. Cortex* **31**, 5165–5187 (2021).
16. Zhao, J. *et al.* Gravity-dependent choice of frame of reference in the posterior parietal cortex. *Curr. Biol.* **35**, 4882-4897.e6 (2025).
17. Mimica, B., Dunn, B. A., Tombaz, T., Bojja, V. P. T. N. C. S. & Whitlock, J. R. Efficient cortical coding of 3D posture in freely behaving rats. *Science* **362**, 584–589 (2018).
18. Soma, S. *et al.* Ipsilateral-dominant control of limb movements in rodent posterior parietal cortex. *J. Neurosci.* **39**, 485–502 (2018).
19. Mimica, B. *et al.* Behavioral decomposition reveals rich encoding structure employed across neocortex in rats. *Nat. Commun.* **14**, 3947 (2023).
20. Lacquaniti, F., Guigon, E., Bianchi, L., Ferraina, S. & Caminiti, R. Representing spatial information for limb movement: role of area 5 in the monkey. *Cereb. Cortex* **5**, 391–409 (1995).
21. Semedo, J. D., Zandvakili, A., Machens, C. K., Yu, B. M. & Kohn, A. Cortical areas interact through a communication subspace. *Neuron* **102**, 249-259.e4 (2019).
22. MacDowell, C. J. *et al.* Multiplexed subspaces route neural activity across brain-wide networks. *Nat. Commun.* **16**, 3359 (2025).
23. Imamura, H., Imamura, F., Hira, R., Isomura, Y. & Hira, R. Independence and coherence in temporal sequence computation across the fronto-parietal network. *bioRxiv* 2025.08.25.672149 (2025) doi:10.1101/2025.08.25.672149.
24. Stringer, C. *et al.* Spontaneous behaviors drive multidimensional, brainwide activity. *Science* **364**, 255 (2019).

25. Musall, S., Kaufman, M. T., Juavinett, A. L., Gluf, S. & Churchland, A. K. Single-trial neural dynamics are dominated by richly varied movements. *Nat. Neurosci.* **22**, 1677–1686 (2019).
26. Reitman, M. E. *et al.* Norepinephrine links astrocytic activity to regulation of cortical state. *Nat. Neurosci.* **26**, 579–593 (2023).
27. Voitov, I. & Mrsic-Flogel, T. Cortical feedback loops bind distributed representations of working memory. *Nature* **608**, 381–389 (2022).
28. Raut, R. V. *et al.* Arousal as a universal embedding for spatiotemporal brain dynamics. *Nature* **647**, 454–461 (2025).
29. Yu, C.-H., Stirman, J. N., Yu, Y., Hira, R. & Smith, S. L. Diesel2p mesoscope with dual independent scan engines for flexible capture of dynamics in distributed neural circuitry. *Nat. Commun.* **12**, 6639 (2021).
30. Hira, R. *et al.* Mesoscale functional architecture in medial posterior parietal cortex. *elife* 10.7554/eLife.105213.1 (2025) doi:10.7554/eLife.105213.1.
31. Hira, R. *et al.* Open-source modular field-programmable gate array system for two-photon mesoscope enabling multiarea, multidepth neural activity recording and lifetime imaging. *Neurophotonics* **13**, 015013 (2026).
32. Marshall, J. D. *et al.* Continuous whole-body 3D kinematic recordings across the rodent behavioral repertoire. *Neuron* **109**, 420-437.e8 (2021).
33. Dunn, T. W. *et al.* Geometric deep learning enables 3D kinematic profiling across species and environments. *Nat. Methods* **18**, 564–573 (2021).
34. Stringer, C. *et al.* Rastermap: a discovery method for neural population recordings. *Nat. Neurosci.* **28**, 201–212 (2025).
35. Chaudhuri, R., Gerçek, B., Pandey, B., Peyrache, A. & Fiete, I. The intrinsic attractor manifold and population dynamics of a canonical cognitive circuit across waking and sleep. *Nat. Neurosci.* **22**, 1512–1520 (2019).
36. Zomorodian, A. & Carlsson, G. Computing persistent homology. *Discrete Comput. Geom.* **33**, 249–274 (2005).

37. Bubenik, P. Statistical topological data analysis using persistence landscapes. *arXiv [math.AT]* (2012).
38. Proske, U. & Gandevia, S. C. The proprioceptive senses: their roles in signaling body shape, body position and movement, and muscle force. *Physiol. Rev.* **92**, 1651–1697 (2012).
39. Peyrache, A., Lacroix, M. M., Petersen, P. C. & Buzsáki, G. Internally organized mechanisms of the head direction sense. *Nat. Neurosci.* **18**, 569–575 (2015).
40. McNaughton, B. L., Battaglia, F. P., Jensen, O., Moser, E. I. & Moser, M.-B. Path integration and the neural basis of the "cognitive map." *Nat. Rev. Neurosci.* **7**, 663–678 (2006).
41. Yoon, K. *et al.* Specific evidence of low-dimensional continuous attractor dynamics in grid cells. *Nat. Neurosci.* **16**, 1077–1084 (2013).
42. Gardner, R. J. *et al.* Toroidal topology of population activity in grid cells. *Nature* **602**, 123–128 (2021).
43. Dombeck, D. A., Khabbaz, A. N., Collman, F., Adelman, T. L. & Tank, D. W. Imaging large-scale neural activity with cellular resolution in awake, mobile mice. *Neuron* **56**, 43–57 (2007).
44. Hoogland, T. M., De Gruijl, J. R., Witter, L., Canto, C. B. & De Zeeuw, C. I. Role of synchronous activation of cerebellar Purkinje cell ensembles in multi-joint movement control. *Curr. Biol.* **25**, 1157–1165 (2015).
45. Najafi, F., Giovannucci, A., Wang, S. S.-H. & Medina, J. F. Sensory-driven enhancement of calcium signals in individual Purkinje cell dendrites of awake mice. *Cell Rep.* **6**, 792–798 (2014).
46. Voigts, J. & Harnett, M. T. Somatic and dendritic encoding of spatial variables in retrosplenial cortex differs during 2D navigation. *Neuron* **105**, 237-245.e4 (2020).
47. Daigle, T. L. *et al.* A Suite of Transgenic Driver and Reporter Mouse Lines with Enhanced Brain-Cell-Type Targeting and Functionality. *Cell* **174**, 465-480.e22 (2018).

48. Oomoto, I. *et al.* Protocol for cortical-wide field-of-view two-photon imaging with quick neonatal adeno-associated virus injection. *STAR Protoc.* **2**, 101007 (2021).
49. Zhang, Y. *et al.* Fast and sensitive GCaMP calcium indicators for imaging neural populations. *Nature* **615**, 884–891 (2023).
50. Hira, R. *et al.* Spatiotemporal dynamics of functional clusters of neurons in the mouse motor cortex during a voluntary movement. *J. Neurosci.* **33**, 1377–1390 (2013).
51. Hattori, R. & Komiyama, T. Longitudinal two-photon calcium imaging with ultra-large cranial window for head-fixed mice. *STAR Protoc.* **3**, 101343 (2022).
52. Oh, S. W. *et al.* A mesoscale connectome of the mouse brain. *Nature* **508**, 207–214 (2014).
53. Thévenaz, P., Ruttimann, U. E. & Unser, M. A pyramid approach to subpixel registration based on intensity. *IEEE Trans. Image Process.* **7**, 27–41 (1998).
54. Pachitariu, M. *et al.* Suite2p: beyond 10,000 neurons with standard two-photon microscopy. *bioRxiv* (2016) doi:10.1101/061507.
55. Vogelstein, J. T. *et al.* Fast nonnegative deconvolution for spike train inference from population calcium imaging. *J. Neurophysiol.* **104**, 3691–3704 (2010).
56. Mathis, A. *et al.* DeepLabCut: markerless pose estimation of user-defined body parts with deep learning. *Nat. Neurosci.* **21**, 1281–1289 (2018).
57. Nath, T. *et al.* Using DeepLabCut for 3D markerless pose estimation across species and behaviors. *Nat. Protoc.* **14**, 2152–2176 (2018).
58. Fischler, M. A. & Bolles, R. C. Random sample consensus: a paradigm for model fitting with applications to image analysis and automated cartography. *Commun. ACM* **24**, 381–395 (1981).
59. Abid, A., Zhang, M. J., Bagaria, V. & Zou, J. Y. Exploring patterns enriched in a dataset with contrastive principal component analysis. *Nat. Commun.* **9**, (2018).
60. Bauer, U. Ripser: efficient computation of Vietoris–Rips persistence barcodes. *J. Appl. Comput. Topol.* **5**, 391–423 (2021).

Supplementary Files

This is a list of supplementary files associated with this preprint. Click to download.

- 6AGMv1.zip
- SupplementaryVideo6.mp4
- Supplementaryinformation.pdf
- SupplementaryVideo1.mp4
- SupplementaryVideo3.mp4
- SupplementaryVideo2.mp4
- SupplementaryVideo4.mp4
- SupplementaryVideo5.mp4